Development of Multifunctional Software for Evaluating the Photonic Properties of New Dielectric Composite Geometries

by

Daniel A. Cogswell

Submitted to the Department of Materials Science and Engineering
in partial fulfillment of the requirements for the degree of

Master of Science in Materials Science

at the

MASSACHUSETTS INSTITUTE OF TECHNOLOGY

June 2006

© Massachusetts Institute of Technology 2006. All rights reserved.

Author . . . .
Department of Materials Science and Engineering
May 18, 2006

Certified by. . . . .
W. Craig Carter
Thomas Lord Professor of Materials Science and Engineering
Thesis Supervisor

Accepted by . . . .
Samuel M. Allen
POSCO Professor of Physical Metallurgy
Chair, Departmental Committee on Graduate Students

Development of Multifunctional Software for Evaluating the Photonic Properties of New Dielectric Composite Geometries

by

Daniel A. Cogswell

Submitted to the Department of Materials Science and Engineering
on May 18, 2006, in partial fulfillment of the
requirements for the degree of
Master of Science in Materials Science

Abstract

Software was developed for solving Maxwell's equations using the finite-difference time-domain method, and was used to study 2D and 3D dielectric composites. The software was written from the ground up to be fast, extensible, and generalized for solving any finite difference problem. The code supports parallelization, allowing solutions to be obtained quickly using a beowulf cluster. An extension to the basic FDTD plane wave source was derived, allowing for the creation of angled, periodic, unidirectional plane waves on a square grid. 1D photonic crystal stacks were arranged in a square array and it was discovered that sizeable bandgaps for 2D and 3D geometries appear along the principle axes for different polarizations of the structure. Furthermore, bandgaps in different directions and polarizations could be made to overlap for reasonably large frequency ranges. The structure show promise for use as a low-threshold lasing and may be optimized to produce a complete photonic bandgap.

Thesis Supervisor: W. Craig Carter
Title: Thomas Lord Professor of Materials Science and Engineering

Acknowledgments

I would like to thank Craig Carter and Karlene Maskaly for guiding me through this work. Craig has always provided sound advice, creative ideas, and encouragement, and Karlene had to put up with many long phone calls and thoroughly answered many long emails. The rest of the Carter Lab deserves credit for helping me stay sane, especially when my software wasn't working or when I had to deal with crashing computers. I thank my loving parents, sisters, and small group for encouragement, support, and motivation, and for conversations on things other than research. I particularly appreciated family vacations to Maine in the summer, and skiing with my Dad in the winter. I also thank the members of the MIT Rowing Club, who taught me that rowing a 2K on an erg is tougher than writing a masters thesis. And lastly, I send appreciation to the Chicago White Sox and Boston Red Sox for their World Series Championships that kept me in good spirits during tough times.

Contents

Contents **7**

List of Figures **9**

1 Introduction **13**

1.1 Maxwell's Equations 13

1.1.1 Coulomb's Law 14

1.1.2 Gauss's Law 15

1.1.3 Ampere's Law 17

1.1.4 Faraday's Law 18

1.1.5 Maxwell's Equations 20

1.2 Constitutive Relations 21

1.3 Electromagnetic Plane Waves 22

1.4 Electromagnetic Waves at an Interface 23

1.5 Wave Impedance 25

2 Photonic Crystals **27**

2.1 The photonic bandgap 28

2.2 The quarter wavelength stack 29

2.3 Calculating photonic bandgaps 29

3 The Finite-Difference Time Domain Approach **33**

3.1 Finite Differences 33

3.2 TE and TM Modes 34

3.3 The Yee Algorithm 35
3.4 Boundary Conditions 36
3.5 Computational Setup 37
3.6 Parallelization 38
3.7 Creating a source with the total/scattered field formulation 41
3.8 An Angled Source 43
3.9 Reflection Error 46

4 2D Dielectric Structures 47
4.1 A new 2D structure 47
4.2 2D Photonic Crystal Performance 50

5 3D Dielectric Structures 53
5.1 A new 3D structure 53
5.2 3D Photonic Crystal Performance 55

6 Discussion 59
6.1 Discussion of results 59
6.2 Discussion of software 60
  6.2.1 Philosophy on Reusable Software 60
  6.2.2 Implementation of Fourier Analysis 61
  6.2.3 A Monte Carlo Method for Optimizing Bandgaps 62
  6.2.4 Public software release 63
6.3 The Future: Multi-physics Modeling 63

A Reflectivity band diagrams for the 2D structure 65

B Reflectivity band diagrams for the 3D structure 73

References 77

List of Figures

1-1 An electromagnetic wave propagating in a vaccum. $\vec{S}$ is the Poynting vector. 23

1-2 Scattering of an electromagnetic wave at a dielectric interface. 25

2-1 Photonic crystals can be periodic in one, two, or three dimensions. Colors represent materials with different dielectric constants[1]. 28

3-1 There are two independent polarization modes, TE and TM, which occur in 2D electromagnetic simulations. 34

3-2 The 3D Yee grid[2]. 35

3-3 The computational setup for calculating the reflectivity band diagram of a dielectric structure. 39

3-4 An increase in performance is observed with a parallelized FDTD simulation. A point of diminishing returns is reached for a large number of processors such that adding an additional processor does not significantly affect the running time of the simulation. 41

3-5 A Yee gridding of the electric and magnetic fields for a 2D TE mode electromagnetic simulation. The total/scattered field formulation is used to create a unidirectional, transparent source. 43

3-6 Generation of a unidirectional angled plane wave with wavelength λ and angle θ. 45

4-1 The 2D structure that was investigated consists of periodically arranged quarter wavelength dielectric stacks. The bandgap was measured for two different orientations of the incident wave. 48

4-2 A comparison of the top and side TE bandgaps for the 1D array of dielectric stacks with a coverage fraction of 30%. Significant overlap is observed for TE mode, suggesting that the 2D structure may have a full TE bandgap. 52

5-1 Views from different angles of the 3D dielectric structure that was studied. The structure consists of rectangular-prism dielectric stacks arranged in a square lattice. Characteristic lengths are labeled. d is the width of a column, a_1 is the thickness of a bi-layer, and a_2 is the lattice spacing of the columns. 56

5-2 A comparison of the top and side bandgaps for the square array of dielectric stacks for various coverage fractions. An overlapping bandgap for all three modes is not quite opened, but the results suggest that such an overlap may be possible. Gray boxes are used to illustrate areas of high overlap. 58

A-1 TE bandgap from the top direction of the 2D array of dielectric stacks with $n_1 = 4.5$ and $n_2 = 1.25$ for various coverage fractions (d/a_2). . . 67

A-2 TM bandgap from the top direction of the 2D array of dielectric stacks with $n_1 = 4.5$ and $n_2 = 1.25$ for various coverage fractions (d/a_2). . . 68

A-3 TE bandgap from the side direction of the 2D array of dielectric stacks with $n_1 = 4.5$ and $n_2 = 1.25$ for various coverage fractions (d/a_2). . . 70

A-4 TM bandgap from the side direction of the 2D array of dielectric stacks with $n_1 = 4.5$ and $n_2 = 1.25$ for various coverage fractions (d/a_2). . . 72

B-1 Bandgap from the top direction as a function of coverage for the square array of 3D stacks with $n_1 = 4.5$ and $n_2 = 1.25$. 74

B-2 H_z polarized bandgap from the side direction as a function of coverage for the square array of 3D stacks with $n_1 = 4.5$ and $n_2 = 1.25$. 75

B-3 E_z polarized bandgap from the side direction as a function of coverage for the square array of 3D stacks with $n_1 = 4.5$ and $n_2 = 1.25$. 76

Chapter 1

Introduction

"One scientific epoch ended and another began with James Clerk Maxwell."
-Albert Einstein

1.1 Maxwell's Equations

In 1864, James Clerk Maxwell published a groundbreaking paper titled "A Dynamic Theory of the Electromagnetic Field" in which he synthesized the electrostatics work of Coulomb, Gauss, Faraday, and Ampere to produce a set of equations that govern the propagation of all electromagnetic waves, thereby uniting electricity and magnetism via coupled oscillating fields. He later correctly predicted that such oscillating electric and magnetic fields could exist not just in conductors but in all materials or even in empty space, and that these electromagnetic waves transport energy. Furthermore, Maxwell showed that his equations predicted the speed of electromagnetic waves to be very close to the best experimentally measured speed of light at his time, and correctly concluded that light was an electromagnetic wave. This realization is considered to be one of the greatest scientific discoveries of all time because it paved the way for modern physics and lead to a technological revolution that has reshaped society[3]. Although his speculation proved to be correct, he encountered much criticism from physicists of the time who found his ideas to be outrageous. The following derivation of Maxwell's Equations was adapted from electrodynamics texts written by Jackson and Kong[4, 5].

1.1.1 Coulomb's Law

Charles-Augustin de Coulomb, in 1781, showed that he had produced a law which describes the force of attraction between charged particles. His work has three important consequences which nicely parallel Newton's equation of gravitational attraction. Coulomb showed that the force between charged particles acted along a straight line between the particles, varied as the magnitude of the charges and the inverse square of the distance between the particles, and that the net force acting on a particle was the vector sum of forces from all surrounding charged particles (i.e. a superposition principle). Coulomb's Law is:

$$\vec{F} = \frac{kq_1q_2}{|\vec{r}|^2}\hat{r} \tag{1.1}$$

where $\vec{F}$ is the force vector, k is a constant and q_1 and q_2 are the charges of the particles separated in space by a vector $\vec{r}$. The hat notation (i.e. $\hat{r}$) denotes a normalized vector. The direction of the force is determined by the sign of the charges – like charges repel and unlike charges attract. Interestingly, the definition of positive and negative charge used today was chosen somewhat arbitrarily by Benjamin Franklin who was fascinated with electricity and who first demonstrated charge conservation experimentally[6].

Having obtained a force law for charged particles, it is useful to define the electric field. It is appropriate to think of electrostatic attraction as occurring via a field like gravity – each charged particle creates a field throughout all of space that other particles feel and react to. The electric field created by a point charge q is defined as the force acting on a unit charge that is placed at at distance from the point charge:

$$\vec{E} = \frac{\vec{F}}{q} \tag{1.2}$$

The force term is defined by Coulomb's Law [Eq. 1.1], and thus the electric field experienced by a unit charge (i.e. $q_2 = 1$) due to the point charge q is:

$$\vec{E} = \frac{kq}{|\vec{r}|^2}\hat{r} \tag{1.3}$$

It is important to note that there is one small flaw with Coulomb's Law. It assumes that there is instantaneous communication between the two point charges that are interacting via electric fields, but Maxwell showed that the fields travel at the speed of light. If the charges are travelling close to the speed of light, Einstein's theory of relativity must be considered and we would have to turn to the field of quantum electrodynamics.

1.1.2 Gauss's Law

Gauss's Law relates the electric flux through a closed surface to the charge enclosed by the surface. Gauss's Law can be derived from Coulomb's Law by considering the flux of the electric field, Φ_E, through a closed surface. This flux is represented by a surface integral:

$$\Phi_E = \oint_S \vec{E} \cdot \hat{n}\, dA \tag{1.4}$$

where dA is a small area patch on a closed Gaussian surface and $\hat{n}$ is the surface normal of that patch. For any charges placed outside the surface, the net flux through the surface will be zero because every imaginary field line that enters the surface will eventually leave the surface. If the point charge q is contained within the surface, field lines only pierce the surface once and the integral is not zero. If dA is projected onto a sphere, the solid angle $d\Omega$ subtended by the patch, located at a distance r from the origin, is defined as the surface area of the patch when projected onto a unit sphere with normal $\hat{n}_s$:

$$d\Omega = \frac{\hat{n}_s \cdot \hat{n}\, dA}{r^2} \tag{1.5}$$

If θ is the angle between the surface normal of the patch and that of the sphere, that is, the angle between $\hat{n}$ and $\hat{n}_s$, then $\hat{n}_s \cdot \hat{n}\, dA = cos\theta\, dA$ and thus $r^2\, d\Omega = cos\theta\, dA$.

Evaluating the surface integral [Eq. 1.4]:

$$\oint_S \vec{E} \cdot \hat{n}\, dA = \oint_S \frac{kq}{r^2}\, dA = \oint_S kq\, d\Omega \tag{1.6}$$

Because there are 4π steradians in a sphere:

$$\oint_S \vec{E} \cdot \hat{n}\, dA = 4\pi kq \tag{1.7}$$

which is Gauss's Law. The law reveals that the flux through any Gaussian surface depends only on the amount of charge that lies within the surface. If the charge exists in the form of a charge density $\rho(\vec{r})$ rather than a collection of point charges, the law can be written as:

$$\oint_S \vec{E} \cdot \hat{n}\, dA = 4\pi k \int_V \rho(\vec{r})\, dV \tag{1.8}$$

Gauss's Law [Eq. 1.7] can be expressed in differential form by application of the divergence theorem[1]:

$$\oint_S \vec{E} \cdot \hat{n}\, dA = 4\pi k \int_V \rho(\vec{r})\, dV = \int_V \nabla \cdot \vec{E}\; dV \tag{1.10a}$$

$$\int_V \left(\nabla \cdot \vec{E} - 4\pi k\rho\right)\, dV = 0 \tag{1.10b}$$

Equation 1.10b can only be true if:

$$\nabla \cdot \vec{E} = 4\pi k\rho \tag{1.11}$$

The issue of units in electromagnetism is complicated. Several systems are commonly used, and they each assign different units and magnitudes to the constants that appear in electrostatics and electrodynamics equations. A good discussion of the different systems can be found in the appendix of Jackson's electrodynamics textbook.

---

[1] The divergence theorem describes a transformation between a surface integral and volume integral for a vector field F [7]:

$$\oint_S \vec{F} \cdot \hat{n}\, dA = \int_V \nabla \cdot \vec{F}\; dV \tag{1.9}$$

For the SI system, the constant k is defined as $k = \frac{1}{4\pi\varepsilon_0}$ where ε_0 is the permittivity of free space. Gauss's Law then becomes:

$$\nabla \cdot \vec{E} = \frac{\rho}{\varepsilon_0} \tag{1.12}$$

1.1.3 Ampere's Law

The relationship between magnetic flux density $\vec{B}$ and a steady state current I flowing through a wire was measured by Ampere. He found the following inverse square relationship which parallels Coulomb's law:

$$d\vec{B} = kI\frac{d\vec{l} \times \hat{r}}{|\vec{r}|^2} \tag{1.13}$$

k is a constant[2], and $d\vec{l}$ is a line element pointing in the direction of the current flow. $\vec{r}$ is a vector from the line element to the point where the magnetic flux is to be determined, and $\hat{r}$ is a unit vector. The equation can be integrated to obtain:

$$\vec{B} = \frac{\mu_0}{4\pi}\int_V \vec{J} \times \frac{\hat{r}}{|\vec{r}|^2}\, dV \tag{1.14}$$

where $\vec{J}$ is the current density. This equation can be simplified[3]:

$$\vec{B} = \frac{\mu_0}{4\pi}\int_V \vec{J} \times \left(-\nabla\frac{1}{|\vec{r}|}\right) dV \tag{1.16a}$$

$$\vec{B} = \frac{\mu_0}{4\pi}\nabla \times \int_V \vec{J}\frac{1}{|\vec{r}|}\, dV \tag{1.16b}$$

and because the divergence of a curl is zero:

$$\nabla \cdot \vec{B} = 0 \tag{1.17}$$

---

[2] For the SI units system, $k = \mu_0 4\pi$

[3] The following equality is used for simplification:

$$\frac{1}{|\vec{r}|^2}\hat{r} = -\nabla\left(\frac{1}{|\vec{r}|}\right) \tag{1.15}$$

A relationship involving the curl of $\vec{B}$ can also be found from equation 1.16b:

$$\nabla \times \vec{B} = \frac{\mu_0}{4\pi} \nabla \times \nabla \times \int_V \frac{\vec{J}}{|\vec{r}|} dV \tag{1.18}$$

Simplification of the above equation will not be presented. It is recommended that the reader consult Jackson's electrodynamics text for a thorough treatment of the solution[4]. Eq. 1.18 can be simplified to a simple relation which is Ampere's Law in differential form:

$$\nabla \times \vec{B} = \mu_0 \vec{J} \tag{1.19}$$

This relationship can be expressed in integral form with the application of Stokes theorem[4]:

$$\int_S \left(\nabla \times \vec{B}\right) \cdot \hat{n}\, dA = \mu_0 \int_S \vec{J} \cdot \hat{n}\, dA \tag{1.21a}$$

$$\oint_C \vec{B} \cdot d\vec{l} = \mu_0 \int_S \vec{J} \cdot \hat{n}\, dA \tag{1.21b}$$

$$\oint_C \vec{B} \cdot d\vec{l} = \mu_0 I \tag{1.21c}$$

Equation 1.21c expresses Ampere's discovery that looping magnetic flux is created and is proportional to the electric current flowing through a loop.

1.1.4 Faraday's Law

All but Faraday's Law were derived from steady state observations. Faraday's time-dependent observations were what later inspired Maxwell to realize that electric and magnetic fields were closely related and lead to Maxwell's famous modification of Ampere's Law. Faraday discovered that a changing magnetic flux induces a looping electric current. He observed temporary variations in a steady-state current flowing

---

[4] Stokes' theorem describes the equality of a line integral and a surface integral[7]:

$$\int_S \left(\nabla \times \vec{F}\right) \cdot \hat{n}\, dA = \oint_C F \cdot \hat{t}\, ds \tag{1.20}$$

S is a surface with normal $\hat{n}$, C is a closed path on S with tangent $\hat{t}$, and $\vec{F}$ is a vector field.

through a circuit as current in a nearby circuit was turned on or off, or if the second circuit was moved relative to the first. He also observed temporary variations in current if a permanent magnet was moved into or out of the circuit. His observations can be expressed as:

$$\xi = -k\frac{d\Phi_B}{dt} \tag{1.22}$$

where ξ is the electromotive force, k is a constant, and Φ_B is the magnetic flux through a surface. The magnetic flux can be expressed as a surface integral of the magnetic flux density $\vec{B}$:

$$\Phi_B = \int_S \vec{B} \cdot \hat{n}\, dA \tag{1.23}$$

Furthermore, the electromotive force ξ around the loop is the line integral of the electric field:

$$\xi = \int_C \vec{E} \cdot d\vec{l} \tag{1.24}$$

Equations 1.22, 1.23, and 1.24 are now combined:

$$\xi = \int_C \vec{E} \cdot d\vec{l} = -k\frac{d\Phi_B}{dt} \tag{1.25}$$

$$\int_C \vec{E} \cdot d\vec{l} = -k\frac{d}{dt}\int_S \vec{B} \cdot \hat{n}\, dA \tag{1.26}$$

If we assume $\vec{E}$ and $\vec{B}$ are in the same reference frame so that relativistic effects can be ignored, Stokes's theorem can be applied to the left side of equation 1.26 to obtain the differential form of Faraday's Law. The constant k disappears because it is equal to unity in the SI system:

$$\int_S \left(\nabla \times \vec{E} + \frac{\partial \vec{B}}{\partial t}\right) \cdot \hat{n}\, dA = 0 \tag{1.27a}$$

$$\nabla \times \vec{E} + \frac{\partial \vec{B}}{\partial t} = 0 \tag{1.27b}$$

1.1.5 Maxwell's Equations

A conservation law can be written for a flux of charge, since charge is a conserved quantity:

$$\frac{\partial \rho}{\partial t} = -\nabla \cdot \vec{J} \tag{1.28}$$

The equation states that the accumulation of charge ρ at a point is the negative divergence of the electric current at the point – equivalent to the amount of charge "arriving" at that point. Maxwell realized this and made a correction to Ampere's Law, which had been derived for the steady state condition $\nabla \cdot \vec{J} = 0$. He used Gauss's Law [Eq. 1.12] to evaluate $\frac{\partial \rho}{\partial t}$ and then substituted the result in the conservation law [Eq. 1.28]. When simplified, the conservation law then becomes:

$$\nabla \cdot \vec{J} + \frac{\partial \rho}{\partial t} = \nabla \cdot \left(\vec{J} + \frac{\partial \vec{D}}{\partial t} \right) = 0 \tag{1.29}$$

Maxwell called $\vec{D}$ the electric displacement field, and it represents the electric flux density in a material[5]. Maxwell then replaced $\vec{J}$ in Ampere's Law (Eq. 1.19) with the term $\vec{J} + \frac{\partial \vec{D}}{\partial t}$, which he called the displacement current, and obtained an equation that describes time-dependent fields:

$$\nabla \times \vec{H} = \vec{J} + \frac{\partial \vec{D}}{\partial t} \tag{1.30}$$

Having obtained a time evolution equation for the electric flux density, Maxwell now had all the pieces necessary to describe electromagnetic waves. Maxwell's equations are:

$$\nabla \times \vec{E} + \frac{\partial \vec{B}}{\partial t} = 0 \tag{1.31a}$$

$$\nabla \times \vec{H} = \vec{J} + \frac{\partial \vec{D}}{\partial t} \tag{1.31b}$$

$$\nabla \cdot \vec{D} = \rho \tag{1.31c}$$

$$\nabla \cdot \vec{B} = 0 \tag{1.31d}$$

---

[5] see section 1.2 for a description of the relationship between $\vec{D}$ and $\vec{E}$.

1.2 Constitutive Relations

Constitutive laws relate the electric field to the electric flux and the magnetic field to the magnetic flux in a material. For linear, isotropic, nondispersive materials the following relationships apply:

$$\vec{D} = \varepsilon \vec{E} \tag{1.32a}$$

$$\vec{B} = \mu \vec{H} \tag{1.32b}$$

where ε is the electrical permittivity tensor of the material and μ the magnetic permeability tensor. Because only isotropic materials were simulated, scalars were used for ε and μ. To eliminate units, both properties are are generally referenced to their values in a vaccum, ε_0 and μ_0:

$$\varepsilon = \varepsilon_r \varepsilon_0 \tag{1.33a}$$

$$\mu = \mu_r \mu_0 \tag{1.33b}$$

ε_r is the relative permittivity and μ_r is the relative permeability. Both are dimensionless scalars, and ε_r is commonly called the dielectric constant. ε_0 is the permittivity of free space and μ_0 is the permeability of free space. These variables are universal physical constants with values of $\varepsilon_0 = 8.854 \times 10^{-12}$ farads/meter and $\mu_0 = 4\pi \times 10^7$ henrys/meter in SI units.

When studying dielectric composites, the index of refraction, n, is often reported instead of the dielectric constant ε_r. The index of refraction represents the ratio of the speed of the electromagnetic wave in a vacuum (i.e. the speed of light) to the speed in the material. The relationship between index of refraction and dielectric constant is:

$$n = \sqrt{\varepsilon_r \mu_r} \tag{1.34}$$

Because the magnetic permeability was held constant for the analysis below, the relative permeability μ_r is unity, and the index of refraction only depends on the dielectric constant:

$$n = \sqrt{\varepsilon_r} \tag{1.35}$$

1.3 Electromagnetic Plane Waves

The solutions to Maxwell's equations give many important insights into the behavior of electromagnetic waves in matter. To begin with, the equations have a travelling plane wave solution[6] of the form $e^{i(\vec{k}\cdot\vec{x}-\omega t)}$. The existence of a travelling plane wave solution explains why electromagnetic waves such as radio waves, infrared, light, ultraviolet rays, and x-rays exist and are able to transport energy through space. Maxwell realized that electric and magnetic fields hold potential energy much like mechanical springs and that the oscillations of the fields allowed them to travel and transport energy.

Figure 1-1 shows the magnitudes of the electric and magnetic field for an electromagnetic wave propagating in a vaccum. The wave propagates in the direction of the Poynting vector $\vec{S}$:

$$\vec{S} = \vec{E} \times \vec{H} \tag{1.36}$$

The Poynting vector defines the direction of energy flow, and its magnitude expresses the energy flux rate, or intensity of the wave (expressed in units of $\frac{energy}{area\cdot time}$). The magnitude of the Poynting vector is used in Section 3.5 to measure the reflectivity of dielectric structures. Because the magnitude of the instantaneous Poynting vector is time-dependent (c.f. how the fields oscillate in figure 1-1), it is often useful to report the time-averaged Poynting vector. The Poynting vector also plays a crucial role in Poynting's theorems of energy and momentum conservation for electromagnetic fields and systems of charged particles.

---

[6] A thorough proof is presented by Jackson[4].

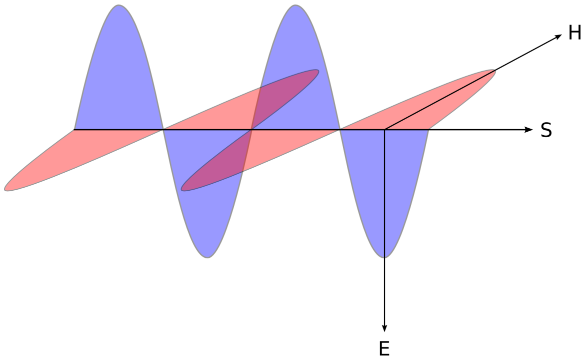

Figure 1-1: An electromagnetic wave propagating in a vaccum. $\vec{S}$ is the Poynting vector.

1.4 Electromagnetic Waves at an Interface

Maxwell's equations can be used to study what happens to an electromagnetic wave at an interface between two materials. The study of optics long preceded Maxwell's work and lead to equations useful for describing optical lenses despite the fact that the nature of light was not well understood. The power of Maxwell's equations is demonstrated in that, in addition to describing electrical and magnetic phenomena, they shed light on all optical phenomena, including topics that had been studied before the time of Maxwell such as reflection, refraction, polarization, total internal reflection, and the Brewster angle.

Figure 1-2 shows an electromagnetic wave being scattered at an interface between materials with indices of refraction n_1 and n_2. The incident wave is partially reflected and partially refracted (transmitted). Wave interactions at an interface obey the phase matching condition, which states that the tangential components of the wave vector, $\vec{k}_t$, are conserved at a boundary[5]. The wave vector $\vec{k}$ points in the same direction as the Poynting vector but its magnitude is the wavenumber, $\frac{2\pi}{\lambda}$. The phase matching condition, which can be derived from Maxwell's equations, has several important consequences. First, the kinematics of electromagnetic wave scattering at an interface can be solved. Conservation of $\vec{k}_t$ for the reflected wave requires that $\vec{k}_t$ be the same for both the incident and reflected wave and produces the familiar rule that the angle of incidence must equal the angle of reflection. Conservation of $\vec{k}_t$ for the refracted wave yields Snell's Law:

$$n_1 sin(\theta_1) = n_2 sin(\theta_2) \tag{1.37}$$

When a wave propagates from a high refractive index material to a low refractive index material, there will be a critical angle θ_c such that when θ_c is exceeded, the tangential component of the incident wave vector $\vec{k}_t^{inc}$ becomes larger than the total wave vector $\vec{k}$ in the material with index n_2. Thus $\vec{k}_t$ cannot be conserved at the interface for a transmitted wave and the result is total internal reflection. θ_c can be found by solving Snell's Law [Eq. 1.37] with $\theta_2 = 90°$:

$$\theta_c = sin^{-1}\left(\frac{n_2}{n_1}\right) \tag{1.38}$$

Another interesting phenomenon occurs when $\vec{k}_n^{trans} = \vec{k}_n^{inc}$, where $\vec{k}_n$ is the value of the normal component of the wave vector. This condition corresponds to $\vec{k}_n$ being conserved across the interface. In this case, the Fresnel equations [Eq. 1.41] reveal that there is no reflected wave; all waves are transmitted. The angle at which this occurs is θ_b, the Brewster angle, which can be found by solving the Fresnel equations for zero reflectivity and employing Snell's Law. Interestingly, the Brewster angle only exists for TM polarized waves (TM is defined in Section 3.2):

$$\theta_b = tan^{-1}\frac{\left|\vec{k}^{trans}\right|}{\left|\vec{k}^{inc}\right|} = tan^{-1}\sqrt{\frac{\varepsilon_2}{\varepsilon_1}} \tag{1.39}$$

The amount of light that is reflected and refracted when a wave scatters at an interface can be calculated from the Fresnel equations. Γ is the reflection coefficient, the ratio of reflected power to incident power, and τ is the transmission coefficient, the ratio of transmitted power to incident power. Γ and τ are related for a lossless material such that:

$$\Gamma + \tau = 1 \tag{1.40}$$

The values of the reflection coefficient depend on the polarization of the incident

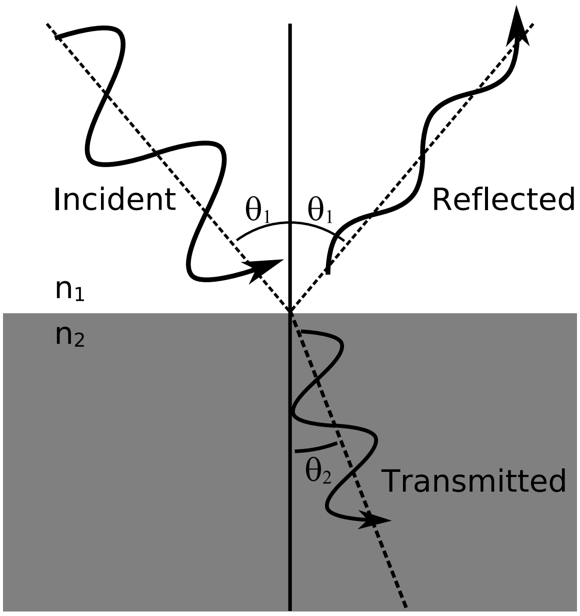

Figure 1-2: Scattering of an electromagnetic wave at a dielectric interface.

wave. The Fresnel equations for both the TE and TM polarizations (Section 3.2) are shown below:

$$\Gamma_{TE} = \left(\frac{E_0^{ref}}{E_0^{inc}}\right)^2 = \left(\frac{\frac{n_1}{\mu_1}cos(\theta_1) - \frac{n_2}{\mu_2}cos(\theta_2)}{\frac{n_1}{\mu_1}cos(\theta_1) + \frac{n_2}{\mu_2}cos(\theta_2)}\right)^2 \tag{1.41a}$$

$$\Gamma_{TM} = \left(\frac{E_0^{ref}}{E_0^{inc}}\right)^2 = \left(\frac{\frac{n_2}{\mu_2}cos(\theta_1) - \frac{n_1}{\mu_1}cos(\theta_2)}{\frac{n_2}{\mu_2}cos(\theta_1) + \frac{n_1}{\mu_1}cos(\theta_2)}\right)^2 \tag{1.41b}$$

E_0^{ref} and E_0^{inc} are the amplitudes of the reflected and incident waves, respectively.

1.5 Wave Impedance

The reflection and transmission of an electromagnetic wave at an interface can also be thought of in terms of wave impedance. The impedance of a material depends on ε and μ, and a difference in impedance between two materials causes electromagnetic waves to be scattered. Such a formulation is useful for understanding the perfectly matched boundary layer described in section 3.4. The wave impedance is the ratio of the transverse electric field to the transverse magnetic field and depends on polarization.

Wave impedance is given as[4]:

$$Z_{TM} = \frac{\omega\mu}{\left|\vec{k}_n\right|} = cos(\theta)\sqrt{\frac{\mu}{\varepsilon}} \tag{1.42a}$$

$$Z_{TE} = \frac{\left|\vec{k}_n\right|}{\omega\varepsilon} = \frac{1}{cos(\theta)}\sqrt{\frac{\mu}{\varepsilon}} \tag{1.42b}$$

$\vec{k}_n$ is the normal component of the incident wave vector and ω is the angular frequency. For normal angles of incidence, the impedance can be simplified to $Z = \sqrt{\frac{\mu}{\varepsilon}}$, and for angles larger than θ_c, the impedance is imaginary[5]. The reflection and transmission coefficients are defined, in terms of the impedance in materials n_1 and n_2 from figure 1-2, as:

$$\Gamma = \frac{Z_1 - Z_2}{Z_1 + Z_2} \tag{1.43a}$$

$$\tau = \frac{2Z_2}{Z_2 + Z_1} \tag{1.43b}$$

Chapter 2

Photonic Crystals

Photonic crystals are periodic arrangements of materials with different dielectric constants that affect the behavior of light. The crystal's geometry exploits the simple reflection and transmission rules for electromagnetic waves as discussed in section 1.4 in such a way that new and useful optical behaviors are produced. Photonic crystals can be used to create perfect dielectric mirrors, light filters and sensors, efficient lasers[8], and waveguides for light. Defects in photonic crystals can be used to trap and control single photons of light[9]. Photonic crystal structures are being used in the development of optical circuits[10], and there has been recent interest in the phenomenon of negative refraction that can be produced with photonic crystals[11].

The study of photonic crystals does not involve more sophisticated concepts than were developed by Maxwell and others in the 1800's. Although Maxwell could have envisioned photonic crystals, they have only recently been studied seriously because advances in manufacturing techniques have allowed the design of structures on the nanoscale.

Because the wavelength of visible light is about 400nm to 700nm, the structures that create novel behavior must be of roughly the same dimensions. An interesting feature of Maxwell's equations is that they are scalable such that the solution is independent of length scale. Thus a solution at one length scale can be scaled and apply to the same system at any other length scale. Thus when simulating a photonic crystal, the geometry should be considered rather than the absolute size of the structure.

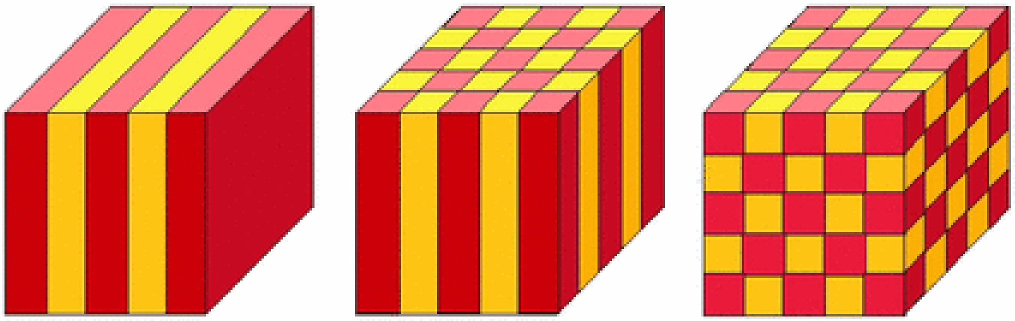

Figure 2-1: Photonic crystals can be periodic in one, two, or three dimensions. Colors represent materials with different dielectric constants[1].

2.1 The photonic bandgap

Photonic crystal geometries are categorized by their periodicity. Figure 2-1 shows how materials with different dielectric constants may be combined to produce geometries that are periodic in one, two, and three dimensions. The periodicity of the crystal is an important factor that controls the crystal's photonic properties[12].

One of the most important features of photonic crystals is that they may have photonic bandgaps. The photonic bandgap is analogous to electronic bandgaps in semiconductors, except that the electrons from solid-state electronics are replaced by photons. A photonic bandgap can be thought of in a couple of ways. A material with a photonic bandgap will reflect all light over a frequency range and transmit none of it, the density of photonic states within the crystal goes to zero in the bandgap, and the modes within the band gap are evanescent (exponentially decaying).

If a photonic crystal reflects light of any polarization incident at any angle, then it has a complete photonic bandgap. 1D and 2D dielectric structures may have a bandgap in one and two directions respectively, but they will not have a complete 3D bandgap because there is no periodicity to scatter electromagnetic waves in at least one direction. 3D photonic crystals are candidates for complete photonic bandgaps, but because they are much harder to manufacture than their 1D or 2D counterparts, they should only be used for applications where a complete bandgap is required. Many dielectric geometries in 1D, 2D, and 3D have been shown to have complete bandgaps for their respective dimensions. Furthermore, many of these structures have been fabricated and the bandgap confirmed experimentally. Commonly studied photonic crystal geometries include the quarter-wavelength stack in 1D, arrays of dielectric circles, circular voids, or linear veins in 2D, and, in 3D, lattices of voids or dielectric spheres[12]. Other more complex 3D geometries have been discovered[1, 13], including some bi-continuous, triply periodic minimal surfaces that can be manufactured by interference lithography.

2.2 The quarter wavelength stack

The 1D photonic stack is a simple structure that exhibits a bandgap and that will be used as the basis for development of more sophisticated 2D and 3D structures in chapters 4 and 5. If the layers of a 1D photonic crystal (leftmost image, figure 2-1) are chosen such that light of wavelength λ travels a distance $\lambda/4$ in each layer, the structure will have a bandgap at normal angles of incidence and is called a quarter wavelength stack. The bandgap exists because all of the light that is reflected at the boundaries constructively interferes and emerges from the structure perfectly in phase. Consider the phase of a plane wave as it penetrates the structure and is partially reflected at each interface. The light that emerges from the quarter wavelength stack has travelled an integer multiple of $\lambda/2$ in each layer, because it must pass through the layer completely at least twice – once when incident and once when reflected. Additionally when light is travelling in a material with low dielectric constant and is reflected by a material with higher dielectric constant there is a phase change of π. The combined effect of these observations is that all of the light is eventually reflected and exits the structure in phase, producing a bandgap.

2.3 Calculating photonic bandgaps

The calculation of a photonic bandgap requires solving Maxwell's equations for a dielectric structure. Frequency domain and time domain algorithms are two different approaches are commonly used to solve Maxwell's equations, and each method has advantages and disadvantages.

The frequency domain approach involves solving Maxwell's equations for eigenvalues and eigenfunctions, analogous to computing the Bloch wave function in quantum mechanics. It is frequency domain because it determines the wave mode eigenfunction $\vec{H}(r)$ for a specific frequency ω that is directly related to the eigenvalue $(\omega/c)^2$. Maxwell's equations are decoupled to produce a Schrodinger-like equation that can be solved for eigenfunctions and eigenvalues[12]:

$$\nabla \times \left(\frac{1}{\varepsilon(r)} \nabla \times \vec{H}(r) \right) = \left(\frac{\omega}{c} \right)^2 \vec{H}(r) \tag{2.1}$$

The frequency domain is appropriate for determining dispersion relations for photonic crystals and for analysis of the photonic band structure, which describes how the wavelength of a propagating wave varies with frequency.

The time domain solution is obtained by iterating Maxwell's equations through time on a spatial grid. The state of the system is known at a specific time, but not necessarily for any specific frequency. Time domain simulations allow for analysis of where fields concentrate in the system and are useful for measuring transmittance and decay times. Time domain simulations, unlike frequency domain simulations, are not restricted to solving for periodic structures because of the development of absorbing boundaries that effectively create a computational domain extending to infinity. Thus any arbitrary, finite system can be simulated. Unfortunately, unlike frequency domain simulations, time domain simulations do not scale well with changes in grid resolution or system size. Also, in the time domain, closely spaced modes may not be distinguishable if the frequency resolution is not high enough. Such a resolution problem will not happen in the frequency domain because different bands are represented by different eigenvalues.

An advantage of the time domain is the ability to solve for a system's response to all frequencies from just one simulation. In the frequency domain for comparison, a new simulation must be run for each frequency to be investigated. This ability is possible in the time domain because the time domain and frequency domain are related via Fourier transforms. A measurement of the response over all frequencies can be achieved by measuring the system's response to an impuse function, which contains all frequencies. As described by Weaver [14], the function $y(x)$ that describes the response of the system to an input function $f(x)$ is given by the convolution of $f(x)$ with $h(x)$, the response of the system to the impulse function:

$$y(x) = \int_{-\infty}^{\infty} f(\xi)h(x-\xi)\,d\xi \tag{2.2}$$

Chapter 3

The Finite-Difference Time Domain Approach

3.1 Finite Differences

FDTD simulations use the method of centered finite differences to solve differential equations numerically on a grid. At a point $u_{i,j,k}$ in space, the derivatives in the x-direction are approximated from the values at neighboring points using centered differencing:

$$\frac{\partial u}{\partial x} = \frac{u_{i+1,j,k} - u_{i-1,j,k}}{2\triangle x} + O\left[(\triangle x)^2\right] \tag{3.1a}$$

$$\frac{\partial^2 u}{\partial x^2} = \frac{u_{i+1,j,k} - 2u_{i,j,k} + u_{i-1,j,k}}{(\triangle x)^2} + O\left[(\triangle x)^2\right] \tag{3.1b}$$

where Δx is the distance between gridpoints in the x-direction. Equations for derivatives in other directions have the same form. This method is "centered" because one point on either side of $u_{i,j,k}$ is used to compute the derivative. The method is only an approximation of the actual derivative, because the derivative is defined in the limit that the grid spacing goes to zero. The amount of error for centered differencing is proportional to $(\Delta x)^2$, and thus it is second-order accurate. Although the differencing scheme has been presented for spatial derivatives, it will also be used to compute temporal derivatives and will provide second-order accuracy in time.

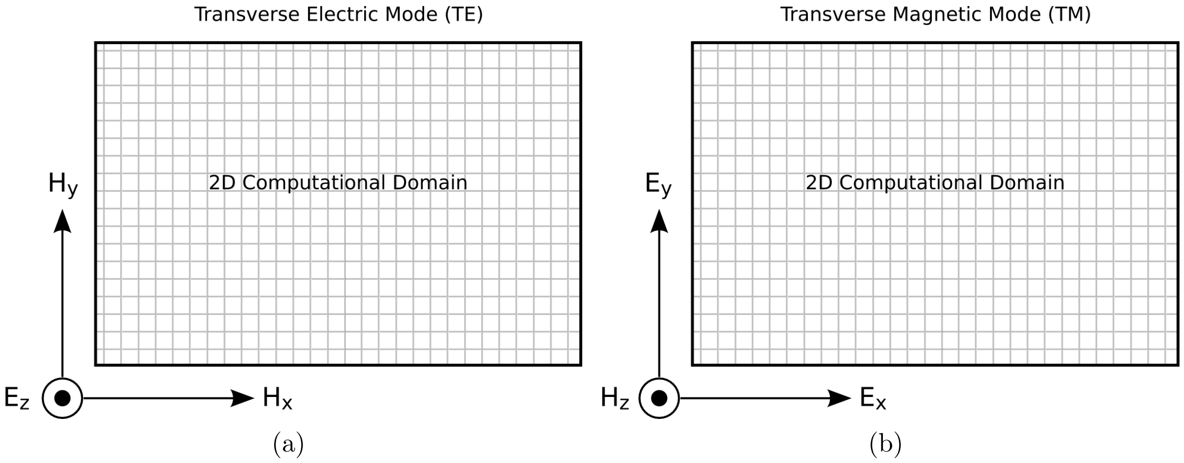

(a) (b)

Figure 3-1: There are two independent polarization modes, TE and TM, which occur in 2D electromagnetic simulations.

3.2 TE and TM Modes

Three vectors are needed to find a solution to Maxwell's curl equations because the cross product in the equations relates three orthogonal vectors. For simulation of a 2D structure there are two possible polarizations to choose from when assigning fields to the 2D computational grid. These two modes are illustrated in figure 3-1, where it can be seen that either H_x, H_y, and E_z or E_x, E_y, and H_z must be chosen as the fields to simulate. The modes are called transverse electric (TE) and transverse magnetic (TM) respectively. Interestingly, it can be derived from Maxwell's equations that the two modes are uncoupled and will not always produce the same behavior. There is disagreement on the naming of the different modes. Joannopoulos, for instance, defines the two modes exactly opposite to the definition used in this work[12].

In terms of the Poynting vector, the two modes represent the only two possible polarizations for a 2D plane wave. Recall that the Poynting vector $\vec{S}$ is the cross product of the $\vec{E}$ and $\vec{H}$ fields. The Poynting vector can be rotated about its axis such that its direction and magnitude remain constant but $\vec{E}$ and $\vec{H}$ are rotated in the plane normal to $\vec{S}$. The different orientations of $\vec{E}$ and $\vec{H}$ represent different polarizations. Polarizations in 3D do not fit into these two categories, and the possible polarizations are related to the point group symmetry of the structure.

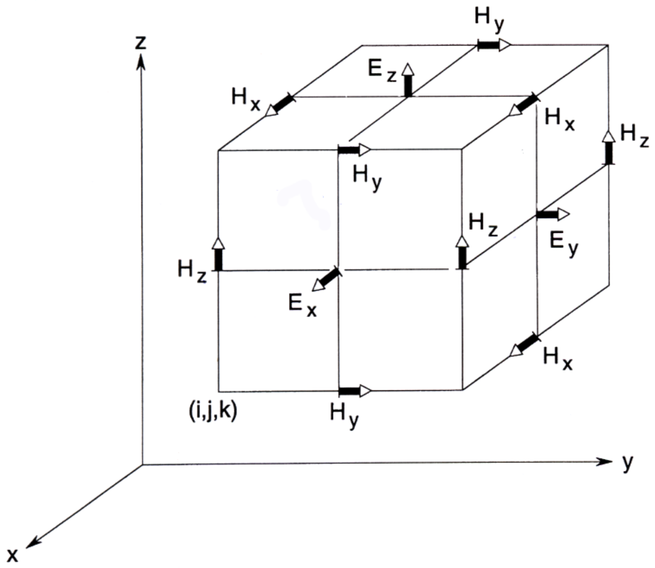

Figure 3-2: The 3D Yee grid[2].

3.3 The Yee Algorithm

In 1966, Kane Yee developed a simple, efficient, and powerful algorithm for numerically solving Maxwell's equations on a finite grid[15]. His algorithm is still widely used today. Yee used a centered differencing scheme [Eq. 3.1a] to solve Maxwell's equations [Eq. 1.31] for both the electric and magnetic fields in space and time. Modeling both fields produces robust solutions and allows for the modeling of electric and magnetic material phenomenon.

A Yee grid for a two dimensional TE mode simulation is illustrated in figure 3-5, and a 3D gridding is shown in figure 3-2. In the Yee grid, the magnetic and electric fields are offset from each other by $\frac{1}{2}$ of a gridpoint. This allows Yee's gridding scheme to implicitly solve Gauss' divergence laws [Eq. 1.31c, 1.31d] because each $\vec{E}$ field point is surrounded by a loop of $\vec{H}$ field points, and each $\vec{E}$ field point is surrounded by a loop of $\vec{H}$ field points. Thus the scheme naturally captures the ideas of Ampere's and Faraday's Laws where flux of an electric or magnetic field through a point induces a loop of either electric or magnetic field, and evolution of Maxwell's equations through time is achieved by employing only the time-dependent curl equations [Eq. 1.31c, 1.31d].

The Yee algorithm uses a leapfrog timestepping approach, where each timestep is divided into two parts. In the first half of the timestep the electric field is updated. In the second half, the magnetic field is calculated using the just updated electric field values. This approach is explicit and second-order accurate in time because it is centered in time. Were forward or backward time differencing used, the solution would only be first-order accurate in time. The Yee discretization of Maxwell's curl equations [Eq. 1.31a, 1.31b] is shown below for the x direction:

$$\begin{aligned}\frac{D_x^{n+\frac{1}{2}}(i+\frac{1}{2},j,k) - D_x^{n-\frac{1}{2}}(i+\frac{1}{2},j,k)}{\Delta t} &= \frac{H_z^n(i+\frac{1}{2},j+\frac{1}{2},k) - H_z^n(i+\frac{1}{2},j-\frac{1}{2},k)}{\Delta y} \\ &\quad - \frac{H_y^n(i+\frac{1}{2},j,k+\frac{1}{2}) - H_y^n(i+\frac{1}{2},j,k-\frac{1}{2})}{\Delta z}\end{aligned}$$

$$\begin{aligned}\frac{B_x^{n+1}(i,j+\frac{1}{2},k+\frac{1}{2}) - B_x^n(i,j+\frac{1}{2},k+\frac{1}{2})}{\Delta t} &= \frac{E_y^{n+\frac{1}{2}}(i,j+\frac{1}{2},k+1) - E_y^{n+\frac{1}{2}}(i,j+\frac{1}{2},k)}{\Delta z} \\ &\quad - \frac{E_z^{n+\frac{1}{2}}(i,j+1,k+\frac{1}{2}) - E_z^{n+\frac{1}{2}}(i,j,k+\frac{1}{2})}{\Delta y}\end{aligned}$$

The equations for the y and z directions are similar in form. The 2D equations for both the TE and TM mode can be found by eliminating the k index and setting the appropriate fields equal to zero. For TE mode $E_x = E_y = 0$, and for TM mode $H_x = H_y = 0$.

3.4 Boundary Conditions

An absorbing boundary called a perfectly matched layer, or PML, was used in the simulations presented below. This particular boundary condition was developed by Berenger[16]. The PML allows for simulation of an infinite computational domain by attenuating the electromagnetic waves at the boundary with minimal reflection. Terminating the computational domain or introducing an artificial boundary causes the electromagnetic waves to be reflected back into the simulation and inhibited the initial use of FDTD for electromagnetic simulations. Several other absorbing boundary algorithms have been proposed, but Berenger's method remains one of the most accurate, and also damps waves at angles of incidence other than the normal angle.

Berenger's PML exploits the fact that if μ and ε are chosen in two different materials such that the impedance Z (as described in section 1.3) in each material is the same, there will not be any reflection at the interface. Furthermore, the waves can be made to decay with the use of complex values for μ and ε. Berenger's method also involves a field-splitting modification of Maxwell's equations for the gridpoints in the PML boundary layer that is necessary to decay the waves. An implementation of the PML coded by Sullivan was incorporated into the developed code[17].

3.5 Computational Setup

The grid layout used to calculate reflectivity band diagrams of dielectric composites using the finite difference method is illustrated in figure 3-3. A unidirectional plane wave is generated from a line source, and allowed to propagate through a vaccum toward a dielectric structure. The plane wave then interacts with the dielectric structure and is partially reflected and partially transmitted. The amplitude of the reflected and transmitted waves changes, but their frequencies do not. The reflected and transmitted waves are measured at the indicated locations in figure 3-3 after the system has reached steady state. The reflected signal must be measured behind the unidirectional source where only the scattered field exists; both the incident and reflected waves exist in the region between the source and the structure. Measurement of the reflected or transmitted wave involves computing the time-averaged power over a region of gridpoints. The power of an electromagnetic wave is the magnitude of the Poynting vector, $\left|\vec{E}\right|^2$, averaged over time. The reflectivity is the ratio of average reflected power to average incident power, which is the same as the ratio of the time-averaged Poynting vectors. Reflectivity can be expressed as:

$$\Gamma = \frac{\left\langle \frac{1}{n_r} \sum^{n_r} \left| \vec{E}_r \right|^2 \right\rangle}{\left\langle \frac{1}{n_i} \sum^{n_i} \left| \vec{E}_i \right|^2 \right\rangle} \tag{3.3}$$

where $\vec{E}_r$ is the electric field of the reflected wave and $\vec{E}_i$ that of the incident wave. n_r and n_i are the number of gridpoints over which $\left|\vec{E}\right|^2$ is summed in the reflected and incident regions respectively (i.e. spatial averaging). The angled brackets denote time averaging. It should be noted that because $\left|\vec{E}\right| = \left|\vec{H}\right|$ for electromagnetic waves, the reflectivity could also be measured in a similar manner using the magnetic field.

The length of time for which the reflected power is averaged must be constrained to correspond to the passage of an integer number of wavelengths. In this study, 24 periods was found to be sufficient to produce stable results, and transmitted power τ was measured instead of reflected power. Γ was found from the relationship $\Gamma + \tau = 1$, which holds for the perfect dielectrics (i.e. $\sigma = 0$) that were simulated. Measuring the transmitted power produced bandgaps that accurately matched accepted results[18] and transmitted power was measured when calculating the bandgaps in the appendices. Measuring reflected power directly produced results that occasionally deviated slightly from the accepted results. The error was not large, and it is possible that there was an interaction between the reflected waves and the unidirectional source. Although it is supposed to be transparent, the unidirectional source may have slightly interacted with reflected waves.

3.6 Parallelization

The software developed was designed to support massive parallelization. The FDTD approach is easily parallelized for solving general finite difference problems across multiple CPUs. FDTD simulations were parallelized using a divide and conquer approach illustrated in figure 3-4a. This approach is well suited for FDTD because

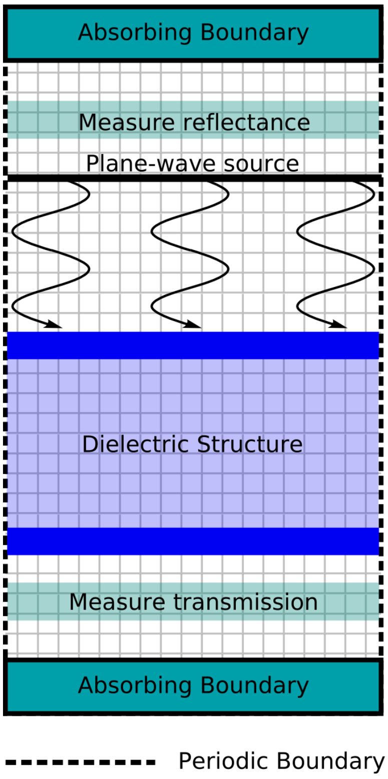
Absorbing Boundary
Measure reflectance
Plane-wave source
Dielectric Structure
Measure transmission
Absorbing Boundary
Periodic Boundary

Figure 3-3: The computational setup for calculating the reflectivity band diagram of a dielectric structure.

the central differencing scheme used requires only that the immediate neighbors of a gridpoint be known in order to advance that gridpoint in time. Thus the large grid illustrated in figure 3-3 can be divided into many smaller subgrids illustrated in figure 3-4a which can be evaluated in parallel by separate processors.

When the original grid is divided into subgrids, each gridpoint at the boundary of two subgrids will be missing a neighbor that it needs and which is stored on an adjacent subgrid, possibly located in the memory of a different CPU. Thus to insure that every gridpoint can be evaluated, each subgrid must exchange boundary gridpoints with its neighboring subgrids at the end of each timestep. Exchange of boundary layers is illustrated with arrows in figure 3-4a. The exchange of boundaries must be completed at the end of each timestep and before the next timestep can be evaluated.

The division of the original large grid into several smaller grids for parallelization was designed to be as transparent as possible for future programmers. Parallelization is implemented for an arbitrary number of processors provided by the user at runtime, and the user does not have to worry about how to divide and distribute the work – the division is performed automatically. The software contains logic for choosing how to divide up the initial large grid into smaller subgrids. The software analyzes the dimensions of the grid to compute which direction to divide it. It is advantageous to divide the grid in such a way as to minimize the size of the boundaries between subgrids because these boundary values will be exchanged, possibly over an ethernet connection which may cause a bottleneck. Each subgrid is a C++ object that keeps track of its neighboring subgrids and therefore knows its absolute position in the overall grid. Items that the programmer places in the grid, such as dielectric structures, plane-wave sources, or measuring points can then be referenced using absolute coordinates and not the relative coordinates for the specific subgrid that the objects exist in. Additionally, objects can span multiple subgrids without needing special attention.

Parallelization was implemented using the Message Passing Interface (MPI) which is a standard language for writing parallel and distributed programs. Because MPI is a communication protocol rather than an implementation, it does not require any specific hardware, operating system, or compiler and works efficiently for many computer configurations. CPUs used for parallel computation can be virtual, located on a multi-processor system using shared memory, or located on computers that are networked together.

Parallelization provides two important advantages for electromagnetic FDTD simulations. First, it provides a measurable speed increase. Figure 3-4b shows that the running time of a 2D FDTD simulation is improved as more CPUs are added. The second advantage of parallelizing FDTD simulations is that it eliminates a potential memory bottleneck. With a single processor simulation, the size of the simulated system is limited by the size of a grid that can fit in the computer's memory without causing a memory overflow. The maximum size of a parallel grid is related to the sum of the memory in every computer being used to solve the problem. If the system becomes too big for one node in the cluster, adding more computers will make the

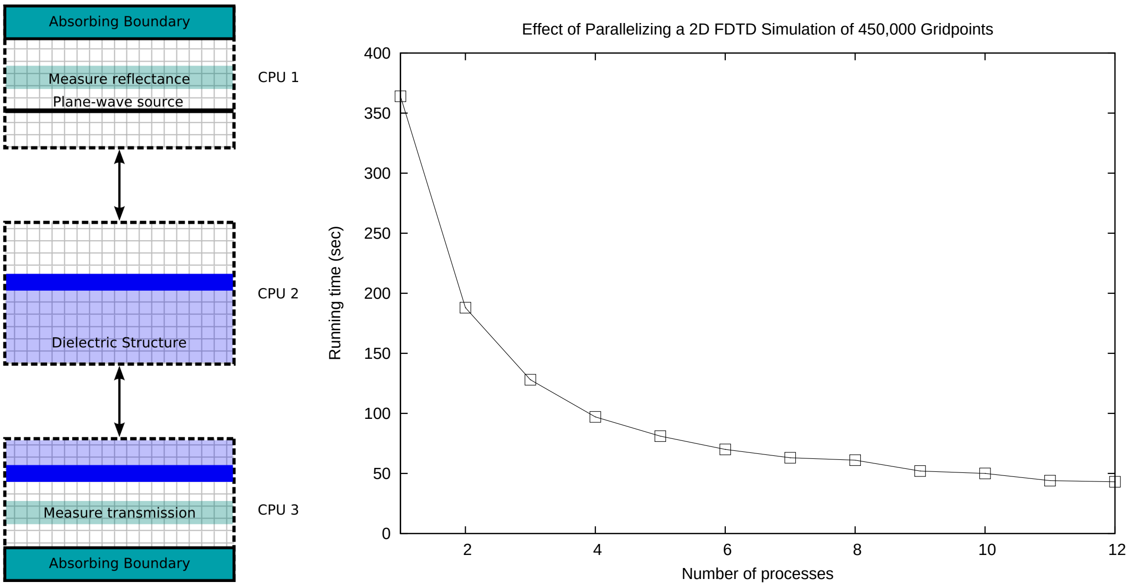

(a) (b)

Figure 3-4: An increase in performance is observed with a parallelized FDTD simulation. A point of diminishing returns is reached for a large number of processors such that adding an additional processor does not significantly affect the running time of the simulation.

problem solvable. In this way it's possible to solve problems on a cluster of computers that are much too large to solve on any one computer in the cluster alone. Additionally, 32-bit memory addressing limits the size of a grid on a single CPU to 4Gb. With this parallelization scheme, the 4Gb limit is avoided on 32-bit machines because the parallelization scheme effectively implements a distributed memory architecture.

3.7 Creating a source with the total/scattered field formulation

A efficient unidirectional, periodic, angled source was derived for use in FDTD electromagnetic simulations. The source was developed by modifying the total-field/scattered-field boundary as described by Taflove and Hagness[2]. This approach is based on the idea that for an electromagnetic plane wave interacting with a dielectric, the total wave is the sum of the incident and scattered parts:

$$\vec{E}_{total} = \vec{E}_{inc} + \vec{E}_{scat} \tag{3.4a}$$

$$\vec{H}_{total} = \vec{H}_{inc} + \vec{H}_{scat} \tag{3.4b}$$

In general, an FDTD electromagnetic simulation will evolve the total field, although it is often the scattered field that is desired for analysis. The incident field is known because it is defined by the programmer as some time-varying field: often a plane wave or Gaussian pulse. The scattered field can only be found by subtracting the incident field from the total field. The simplest way to calculate the scattered field is to run two simulations. One simulation contains the dielectric structure and is used to calculate the total field. The second simulation simulates the incident field on a grid of identical dimensions, but with the dielectric structure replaced by vacuum ($n = 1.0$). The scattered field is found at each timestep by subtracting the incident field from the total field. Although this approach is conceptually simple, it is inefficient. Twice the number of gridpoints and memory are required, resulting in the simulation being slow and possibly causing a memory overflow. If the simulation is run in parallel, twice as many boundary values must be passed between subgrids.

The total/scattered field boundary formulation provides an efficient way of separating the scattered field from the total field and allows for the introduction of non-physical unidirectional transparent sources. A unidirectional source is non-physical because any line or plane of oscillating fields in a physical system will produce a wave that propagates away from the source in all directions. Unidirectionality is effectively achieved by cancelling out the propagation of the wave in one direction, creating a total/scattered field boundary.

Figure 3-5 illustrates the formulation of the total/scattered field for TE polarization. A similar figure applies to the formulation for TM. The formulation corrects inconsistencies that develop at the boundary between a total and scattered field. Such a boundary is illustrated with white and shaded regions in figure 3-5. The boundary is located between gridpoints jb and $jb + 1/2$. Application of the Yee equations re-

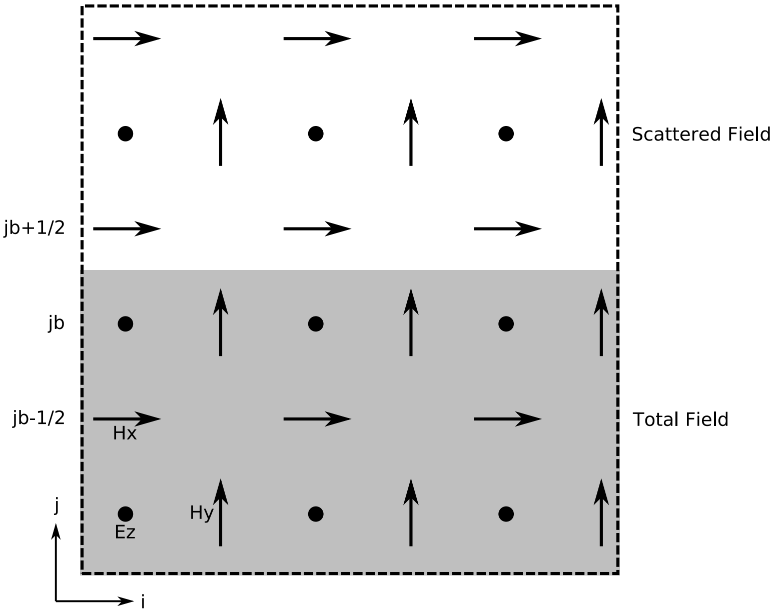

Figure 3-5: A Yee gridding of the electric and magnetic fields for a 2D TE mode electromagnetic simulation. The total/scattered field formulation is used to create a unidirectional, transparent source.

veals that the calculation of E_z points at jb and H_x points at $jb+1/2$ are inconsistent because one point from the scattered field and one point from the total field are used. The inconsistency can be resolved by appropriately adding or subtracting the incident field, which is known by the programmer, after each inconsistent calculation has been made. The correction terms are:

$$E_z^{n+\frac{1}{2}}(i,jb) = E_z^{n+\frac{1}{2}}(i,jb) - \frac{\Delta t}{\varepsilon_0 \Delta x} H_{x,inc}^{n}(i,jb+\frac{1}{2}) \tag{3.5a}$$

$$H_x^{n+1}(i,jb+\frac{1}{2}) = H_x^{n+1}(i,jb+\frac{1}{2}) + \frac{\Delta t}{\varepsilon_0 \Delta x} E_{z,inc}^{n+\frac{1}{2}}(i,jb) \tag{3.5b}$$

3.8 An Angled Source

The general form of a 1D travelling wave with wavelength λ and period T, travelling in the x-direction is:

$$y = sin(kx - wt) \tag{3.6}$$

where $k = \frac{2\pi}{\lambda}$ is the angular wavenumber, x is the position, $w = \frac{2\pi}{T}$ is the angular frequency, and t is time. As time progresses, the amplitude at each x position changes and the wave is observed to propagate. In the case of electromagnetic waves propagating through a vacuum, the velocity at which the wave propagates is the speed of light, c.

In 2D and 3D FDTD electromagnetic simulations, a periodic plane wave can be generated from a line or plane of discrete gridpoints that oscillate in phase, as illustrated in figure 3-3. A line of oscillating fields in 2D and a plane in 3D generate a plane wave because, according to Huygens' principle, all points on a wavefront serve as point sources of spherical secondary wavelets. After a time t, the new position of the wavefront will be that of the surface tangent to these secondary wavelets[19]. Each point on the source line or plane contributes a spherical wavefront to the tangent surface of a plane wave. However, creating an angled incident wave on a square FDTD grid is troublesome. A simple solution would be to place the source line or plane at an angle relative to the grid, but the plane wave source must be periodic so that it is compatible with periodic boundaries. If the source is simply inclined relative to the grid, the source is not periodic because the source is not continuous across the periodic boundaries. The same periodicity argument can be made for keeping the source fixed and simply rotating the dielectric structure – the rotated structure will not be periodic. Placing the source at an angle relative to the grid introduces aliasing as well because an angled line of points cannot be exactly represented on a square grid – the sampling of points along the line will be non-uniform, and the nonuniformity will depend on the angle of the source. Low inclination angles would be particularly troublesome.

If the incident field varies periodically in time along the x-direction of the source line, an angled plane wave will be generated. Because the systems being investigated are periodic in the x-direction, the variation of the field in that direction must also be periodic such that an integer number of wavelengths fits along the x-axis. The consistency rule is:

$$m\lambda = n_x \, sin(\theta) \tag{3.7}$$

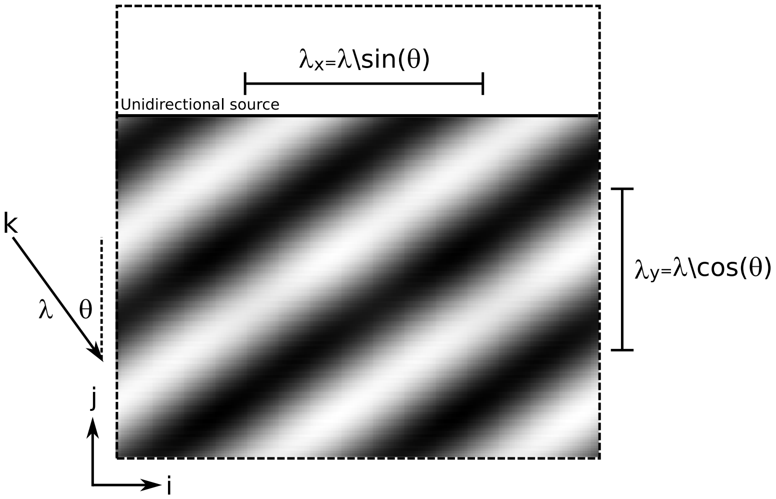

Figure 3-6: Generation of a unidirectional angled plane wave with wavelength λ and angle θ.

where λ is the wavelength of the angled wave generated, m is an integer and n_x is the number of gridpoints in the x-direction. If the condition is not met, the angled wave will not be periodic and will be inconsistent with the boundary conditions.

Figure 3-6 shows a unidirectional, periodic, angled plane wave source for a 2D FDTD simulation. The wavelengths in the x and y directions are labeled as λ_x and λ_y. An equation that describes the amplitude of the 2D plane wave as a function of position (analogous to Eq. 3.6) is:

$$y = sin\,(k_x\, i + k_y\, j - \omega\, t) \tag{3.8a}$$

$$y = sin\left(\frac{2\,\pi}{\lambda_x} i + \frac{2\,\pi}{\lambda_y} j - \frac{2\,\pi}{\lambda}\, c\, t\right) \tag{3.8b}$$

$$y = sin\left(\frac{2\,\pi}{\lambda}\,(i\, sin(\theta) + j\, cos(\theta) - c\, t)\right) \tag{3.8c}$$

When substituted into the total/scattered field equations (Eq. 3.5), the equations for an angled 2D plane wave for TE mode become:

$$E_z(i, jb) = E_z(i, jb) - \frac{1}{2} sin\left(\frac{2\pi}{\lambda}\left(i\, sin(\theta) - \frac{\Delta\, t}{\varepsilon_0 \Delta\, x} cos(\theta) - c\, n\, dt\right)\right) \tag{3.9a}$$

$$H_x(i,jb+\frac{1}{2}) = H_x(i,jb+\frac{1}{2}) + \frac{\Delta t}{\varepsilon_0 \Delta x} sin\left(\frac{2\pi}{\lambda}\left(i\, sin(\theta) - c\,(n+.5)\,dt\right)\right)\frac{1}{cos(\theta)} \tag{3.9b}$$

The $\frac{1}{cos(\theta)}$ term in equation 3.9b projects the angled $H_{x,inc}$ onto the x-axis of the grid's coordinate system. Similar arguments were used to derive angled sources for TM mode and also in 3D.

3.9 Reflection Error

The PML described in section 3.4 is, unfortunately, not a completely perfect absorber and this fact has important consequences for the periodic angled source. Because the PML is terminated at the boundary of the simulation domain, there is a small nonphysical reflection back into the simulation domain. This reflection error, $R(\theta)$, is found to be[2]:

$$R(\theta) = e^{-2\sigma\eta\, d\, cos\theta} \tag{3.10}$$

where η and σ are the characteristic wave impedance and conductivity of the PML. Unfortunately for the angled periodic source, the reflection error increases with the exponential of $cos(\theta)$. This means that as the angle of incidence approaches 90°, the PML becomes completely ineffective. The angle of incidence used in a simulation should be kept as small as possible to minimize reflection error and the angled source should be used cautiously. Reflection error should not prohibit the use of the angled source because there will be very little error for small angles.

Chapter 4

2D Dielectric Structures

4.1 A new 2D structure

A quarter wavelength stack (section 2.2) was used as a starting point for developing a new photonic crystal geometry that may possess desirable optical properties and potentially a complete photonic bandgap. A drawing of a 2D version of the proposed structure is shown in figure 4-1 (Chapter 5 deals with an analogous 3D structure). The design consists of introducing periodic gaps in a 1D quarter wavelength stack, or alternatively, placing rectangular quarter wavelength stacks on a 1D lattice. Figure 4-1 also demonstrates the two configurations for which bandgap calculations were made. Figure 4-1a shows the top configuration, and figure 4-1b shows the side configuration. In both cases, the computational domain was periodic in the direction normal to the incident wave vector. For the top direction, an infinite line of stacks with a finite number of bi-layers was simulated, while for the side configuration a finite number of stacks with an infinite number of bi-layers was simulated.

In all 2D calculations of the top configuration, 4 bi-layers were used for each dielectric stack, as illustrated in figure 4-1. It was observed that the addition of more bi-layers slowed the FDTD simulation but did not significantly change the bandgap of the structure. However, if a smaller dielectric contrast was used, more layers would be required to achieve optical performance comparable to that of an infinite stack.

For the side configuration, each stack effectively contained an infinite number

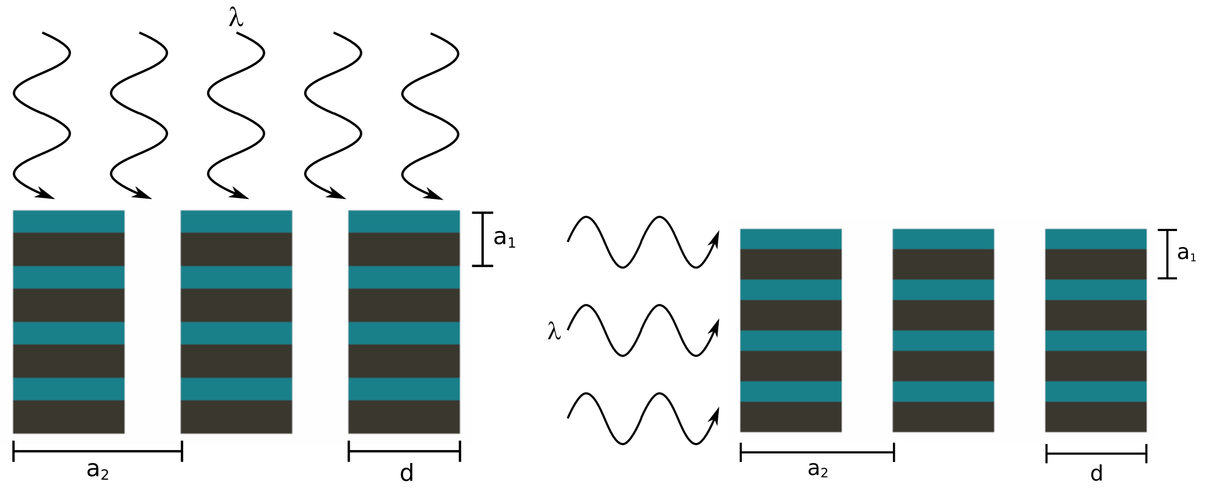

(a) The direction of incident waves when measuring the bandgap from the top.

(b) The direction of incident waves when measuring the bandgap from the side.

Figure 4-1: The 2D structure that was investigated consists of periodically arranged quarter wavelength dielectric stacks. The bandgap was measured for two different orientations of the incident wave.

of bi-layers because the longitudinal axis of stacks lie perpendicular to a periodic boundary. Twenty stacks were used in the non-periodic direction. It was observed that after about ten stacks, the bandgap of the system did not change significantly as more stacks were added.

The proposed photonic crystal geometry presents a difficult challenge in that there are many more variables that must be considered in its design when compared to other 1D and 2D photonic crystal geometries. The most important difference when compared to the quarter wavelength stack is that the presence of gaps in the structure create periodicity in a second direction, forming a 2D photonic crystal. It was hypothesized that the width of the gaps might be controlled so as to produce a bandgap from the side of the crystal. From the side, the structure is similar to a 1D stack where one layer has two sandwiched components and the other layer is air ($n = 1.0$). This structure has also introduced a third component, another major difference when compared to most previously studied photonic crystal geometries that incorporate only two dielectric components.

Several important lengths that characterize the new geometry are illustrated in figure 4-1. They are the bi-layer thickness a_1, the lattice spacing of the columns a_2, and the diameter or width of each column, d. Investigating the effects of each variable independently would be time-consuming, but luckily the system can be simplified by nondimensionalizing several variables. It can be derived from Maxwell's equations (and was also verified computationally) that doubling the system size produces the exact same optical response for wavelengths twice as large – there is no inherent length scale associated with Maxwell's equations. Thus a good approach to characterize the structure is to nondimensionalize the system by fixing the ratio $\frac{a_1}{a_2}$, which can be thought of as an aspect ratio, and to vary the column width, d. The ratio $\frac{d}{a_2}$ will be referred to as coverage fraction, because it represents the fractional area that the dielectric stacks occupy. For all badgaps presented below, $\frac{a_1}{a_2} = \frac{23}{30} = .7667$. This ratio was chosen somewhat arbitrarily because it allowed for integer values of gridpoints for both dimensions and wavelengths. It is likely that the structure will behave differently as the ratio is varied, and the effect of the ratio will be the subject of future work.

Wavelengths are reported in a nondimensional unit of $\frac{\lambda}{a_1}$, where λ is the wavelength and a_1 is the bi-layer thickness. $\frac{\lambda}{a_1}$ characterizes a dielectric stack because scaling the layer thickness will equally scale the quarter wavelength of the stack.

For all 2D studies, the largest realistic dielectric contrast, $\frac{n_1}{n_2}$, was used. A large dielectric contrast allows for fewer bi-layers in the simulation of a photonic stack. Although the 1D stack is by definition infinite, a finite stack of high contrast can have just a few bi-layers and approximate an infinite stack. Maxwell's equations are also dielectric contrast independent; doubling the dielectric constants of the system will produce the same behavior for wavelengths half as large. However, because the system being investigated contains 3 different dielectrics and n_{air} cannot be changed, the absolute values of the dielectric constants will come into play. The effect of absolute index of refraction remains to be investigated. Silicon has one of the highest indices of refraction for a commonly used dielectric at $n = 3.6$, and air has the lowest possible constant at $n = 1$. Thus for the 2D system described in the next section, a dielectric contrast of $\frac{3.6}{1.0}$ was used. The values used for n_1 and n_2 were 4.5 and 1.25 respectively. These values were chosen with $n_2 > n_{air}$ so that the system would contain three components. $n_1 = 4.5$ is high for an index of refraction, but it not completely unrealistic and could be lowered if the number of bi-layers in the stacks was increased.

Unlike other photonic crystal structures that are known to posses full bandgaps, this new geometry has the advantage of potentially being easy to manufacture. Methods are available to make 1D dielectric stacks via deposition processes, and gaps could conceivably be introduced into the the structure with a masking process or with a focused ion beam. The design also naturally lends itself to the introduction of controlled defects. For a 1D quarter wavelength stack, a defect is created by changing the thickness of one of the dielectric layers, and such a defect could be easily introduced during deposition of the layers. The defect layer creates a localized region where frequencies within the photonic bandgap can exist without decaying. The quarter wavelength stacks on each side of the defect essentially act as mirrors and prevent the light from escaping from the defect.

This new photonic crystal geomentry may be suitable for some special applications. The FDTD method has been used to study micropost microcavities[20], which are quarter wavelength stacks with a defect layer that acts as a cavity. The optical thickness of the defect layer can be controlled to define the wavelength of light that is trapped. If a quantum dot is placed in the defect cavity, the quantum dot exhibits enhanced spontaneous emission of a stream of single photons[21]. Single photon sources are necessary for quantum cryptography and quantum computation, and it has been proposed that strategically designed arrays of microposts might be a candidate for a new low-threshold, tunable lasing material. Such a structure with defects might also be useful as a solar collector or tunable light filter.

4.2 2D Photonic Crystal Performance

Bandgaps for the 2D structure were computed using the software described in section 3.5, and important bandgaps are displayed in appendix A. Joannopoulos observed that TE band gaps are favored in a lattice of isolated high-ε regions, and TM band gaps are favored in a connected lattice[12]. Kong also remarks that for a solid dielectric surface, TE waves generally reflect more than TM waves[5]. The structure being investigated consists of isolated stacks, and both trends was observed during TE and TM calculations of the top and side bandgaps.

Following the observations of Joannopoulos and Kong, the top TM bandgap is observed to disappear rather quickly as the periodic gaps are introduced and the structure becomes disconnected (figure A-2). At a coverage fraction of 70% for instance, the bandgap has already closed. For the TE mode however (figure A-1), the top bandgap persists and remains wide, even at low coverage fractions. A sizeable bandgap was found to exist at coverage fractions as low as 10%, as is shown in figure A-1j. The progression of the bandgap with decreasing coverage shows that the bandgap narrows and shifts toward shorter wavelengths: a blue shift. The fact that the bandgap persists reveals the suprising result that, for the top-down TE case, the structure is a perfect dielectric mirror even though it is full of holes in the direction of propagation of the incident light. For the 10% coverage case, consider that the structure is 90% empty space yet maintains a bandgap. The same phenomenon is observed in 3D in chapter 5, and an explanation for why a structure with such a large fraction of holes may act as a perfect mirror is ventured in chapter 6.

Appendix figures A-3 and A-4 show bandgaps calculated from the side for both TE and TM modes, respectively. The shape of the reflectivity plots is noticeably different from the side than from the top for both polarizations. The TE plots in figure A-3 show the existence of several bandgaps that persist over a wide range of coverage fractions. These gaps appear to merge as coverage is decreased. As with the top bandgap, the gaps appear to shift toward the blue frequency range as the coverage fraction is decreased. The primary gap is the widest for coverage fractions around 40%. The trends for TM mode from the side (figure A-4) are similar to TE. Multiple bandgaps are observed at a few coverages but, unlike the TE case, the higher order gaps are narrow and the primary gap is spike-shaped. Like the TE side gap, the TM gap also appears to be largest around 40% coverage. However, unlike TE, the gap does not quite open at very high and very low coverages.

For the structure to have a complete 2D bandgap, it is necessary for a gap to exist

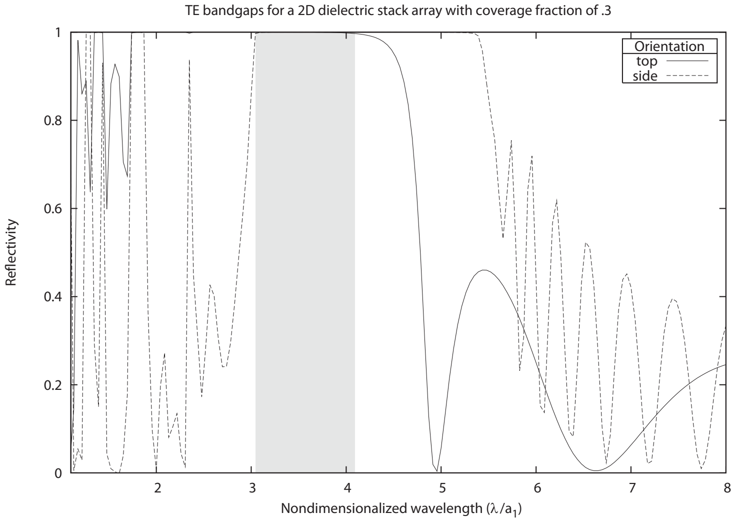

Figure 4-2: A comparison of the top and side TE bandgaps for the 1D array of dielectric stacks with a coverage fraction of 30%. Significant overlap is observed for TE mode, suggesting that the 2D structure may have a full TE bandgap.

for both top and side directions and for both polarizations over the same frequency range. Additionally, the gap must exist for all angles of incidence. Although angle of incidence was not varied (all calculations were performed for normal incidence), it can be concluded that this 2D structure does not have a complete gap because there is no coverage fraction for which the top and side TM bandgaps overlap at a normal angle of incidence. The top TM bandgap provides the most difficulty, appearing only at high coverages where the side bandgaps are small or non-existant.

Significant overlap for the two TE bandgaps is observed and it is possible that the structure may have a complete TE 2D bandgap. Figure 4-2 shows an overlay of the two directional bandgaps for the coverage fraction of 30%, which produced the largest overlap. The overlapping region is highlighted with a grey bar. The fractional width of the overlapping region is approximately 30%, making it a very wide overlap. Generally, a bandgap is considered to be wide when its fractional width, as measured by dividing the width of the bandgap by the value at its center, exceeds 10%. The TM side bandgap overlaps both TE gaps a small amount at 30% coverage, and it is possible that optimizing the aspect ratio of the system might permit this overlap to be increased. However, I am pessimistic that any dimensional changes could be made that will maintain the top TM bandgap to low coverage fractions.

Chapter 5

3D Dielectric Structures

5.1 A new 3D structure

A 3D structure was designed and analyzed using the same strategy as for the 2D structure of section 4.1. The 3D structure, illustrated in figure 5-1, is a square lattice of rectangular-column quarter wavelength stacks. Rectangular columns were chosen over cylindrical columns because the rectangle does not exhibit aliasing effects when scaled on a square grid. If cylindrical columns were represented using the current gridding scheme for instance, the grid resolution would be yet another variable to consider. Cylindrical columns with a large diameter would be well resolved when drawn on a rectangular grid, but those with a small diameter would be blocky and rough. The error associated with representing a cylindrical column on a rectangular grid for FDTD simulations is unknown, although it has been observed that perhaps aliasing does not have much of an effect and instead it is the periodicity of the structure that characterizes the bandgap[1]. Nonetheless, square columns were used to eliminate this potential source of error.

Simulating the structure in 3D presents several challenges not encountered in 2D. First, the running time of the simulation increases due to the fact that the number of gridpoints has increased. The 2D simulations only had to store three field components (Either H_x, H_y, and E_z for TE mode, or E_x, E_y, and H_z for TM mode), but for 3D all six field components (x, y, and z for both $\vec{E}$ and $\vec{H}$) must be stored. Thus in addition to their being more grid points for the third dimension, the equation for evolving each grid point contains more terms and is slower to compute.

Figures 5-1b and 5-1c show the dimensions that were used to characterize the 3D structure. The bird's eye view shows that the the columns have a square cross-section and are arranged on a square lattice. There is 4-fold rotational symmetry along this axis. This means that, if the longitudinal axis of the columns is aligned along the z-axis as shown in the figure, it is not necessary to distinguish between the x-axis side bandgap and y-axis side bandgap because of symmetry. Thus the term "side bandgap" now refers to either the x or y axis.

4-fold rotational symmetry simplifies the system considerably. Without it, the columns would be characterized by two widths, there would be two lattice constants, and bandgaps along all three axes would have to be calculated. Symmetry also allows the system to be nondimensionalized and compared to its 2D counterpart. The 3D structure was nondimensionalized in the same manner as the 2D structure (section 4.1) by setting the aspect ratio $\frac{a_1}{a_2} = \frac{23}{30}$. As with the 2D structure, plane wave wavelengths are presented in nondimensional units of $\frac{\lambda}{a_1}$, but in 3D the coverage becomes $\left(\frac{d}{a_2}\right)^2$. The squaring operation emphasizes that in 3D the the stacks have a 2D cross-section, whereas in 2D the stacks had a 1D cross-section.

Although TE and TM modes were defined as 2D concepts in section 3.2, analogous modes exist in 3D but are dependant on the point group symmetry of the system. Because of the superposition principle of electromagnetic waves, it is possible to break any incident wave into two orthogonally polarized components. Consider the plane wave illustrated in figure 5-1b that is incident upon the top of the array of stacks: the Poynting vector of the plane wave is parallel to the z-axis of the columns, with the $\vec{E}$ field and $\vec{H}$ field in the x-y plane. The dielectric structure has 4-fold symmetry around the z-axis. As the $\vec{E}$ and $\vec{H}$ fields are rotated about the z-axis, the dielectric environment they experience will change with the degree of rotation. After a rotation of 90°, the two fields will be back in identical positions. Because of this rotational symmetry, these two orthogonal polarizations must be equal. Thus the reflectivity of any arbitrarily oriented polarization along the 4-fold axis will be isotropic.

The side configuration has 2-fold rotational symmetry along the incidence axis (either x-axis or y-axis), and thus two polarization conditions exist. If $\vec{E}$ and $\vec{H}$ are restricted to being parallel to principle axes for simplicity, one condition puts the $\vec{E}$ field along the longitudinal axis of the columns (E_z-polarized), and the other puts the H field along the longitudinal axis (H_z-polarized). Because of the principle of superposition of waves, all other polarization angles can be broken into components that are E_z-polarized and H_z-polarized.

5.2 3D Photonic Crystal Performance

The 3D structure, like its 2D counterpart, has indices of refraction of $n_1 = 4.5$ and $n_2 = 1.25$, and bandgaps for the top and side configurations of the structure can be found in Appendix B. As discussed in the previous section, there is no need to specify polarization for the top configuration due to the 4-fold symmetry axis, but two polarizations, E_z and H_z, exist when measuring the side bandgap. The trends observed for the 2D structure appear in analysis of the 3D structure. The top bandgap (figure B-1) exists for high coverage fractions, and decreases in width and shifts toward lower wavelengths as coverage is decreased. Because the top gap persists with decreasing coverage, it suggests that an array of stacks may be a perfect dielectric mirror under certain conditions. When compared to the 2D top bandgaps in Appendix A, the 3D bandgaps appear qualitatively similar to the TE gaps at high coverage, and similar to the TM gaps at low coverage. Recall that coverage fraction for the 3D structure is $\left(\frac{d}{a_2}\right)^2$, so coverage fraction should not be used to directly compare 2D and 3D results. Nonetheless, it is interesting to look for qualitative similarities in the shapes of the 2D and 3D bandgaps. Whether there is any physical explanation for such similarities remains to be investigated.

Bandgaps for H_z polarization are shown in figure B-2 and for E_z polarization in figure B-3. The bandgaps for the two polarizations appear to be qualitatively similar, with a primary bandgap opening at roughly 3 wavelengths for middle to low coverages. The H_z gap is wider than the E_z gap and is also sustained over a larger

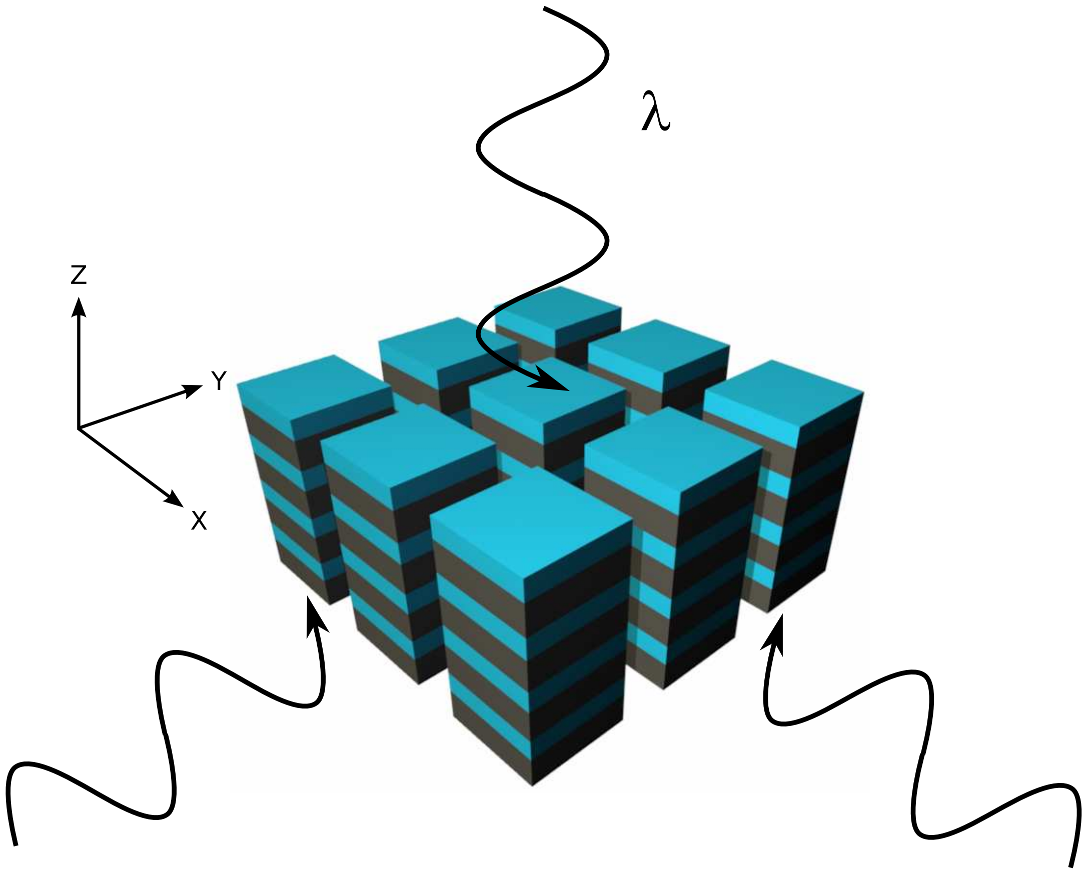

(a) A perspective view of the structure. Incident waves are shown for the top and side configurations.

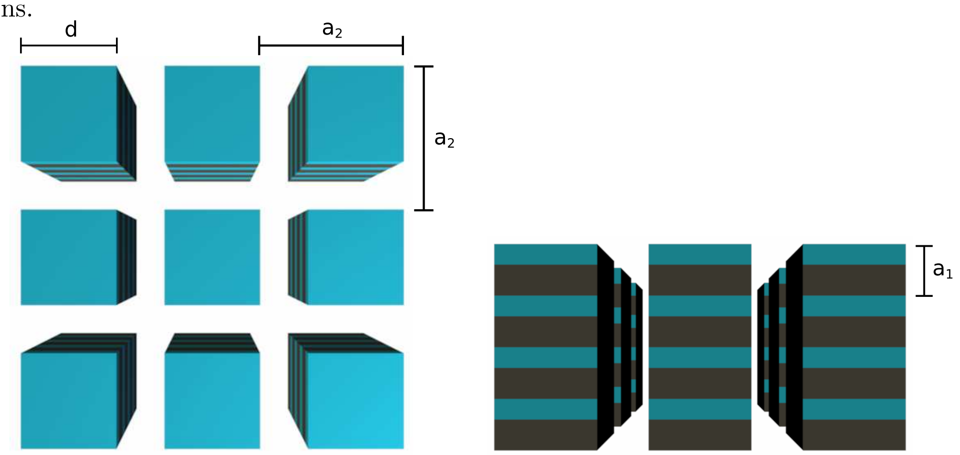

(b) A bird's eye view from the top of the 3D photonic crystal.

(c) The 3D photonic crystal as viewed from the side.

Figure 5-1: Views from different angles of the 3D dielectric structure that was studied. The structure consists of rectangular-prism dielectric stacks arranged in a square lattice. Characteristic lengths are labeled. d is the width of a column, a_1 is the thickness of a bi-layer, and a_2 is the lattice spacing of the columns.

range of coverages. Higher order bandgaps are seen at shorter wavelengths, and they appear to be more significant for the H_z polarization. For several coverages, these side bandgaps overlap with the top bandgap. Figure 5-2 shows an overlay of the top and side bandgaps for the coverages that showed high degrees of overlap. Gray boxes highlight regions of overlap where optimizing architectural parameters might lead to the development of an overlapping bandgap for all three polarizations. The progression from 81% to 64% to 49% coverage shows the E_z gap starting to form while the top gap disappears and shifts to the left. For H_z, the width and position relative to E_z do not vary much. Thus for the aspect ratio chosen, it appears that if an overlapping bandgap exists for this system, it should between 49% and 81% coverage.

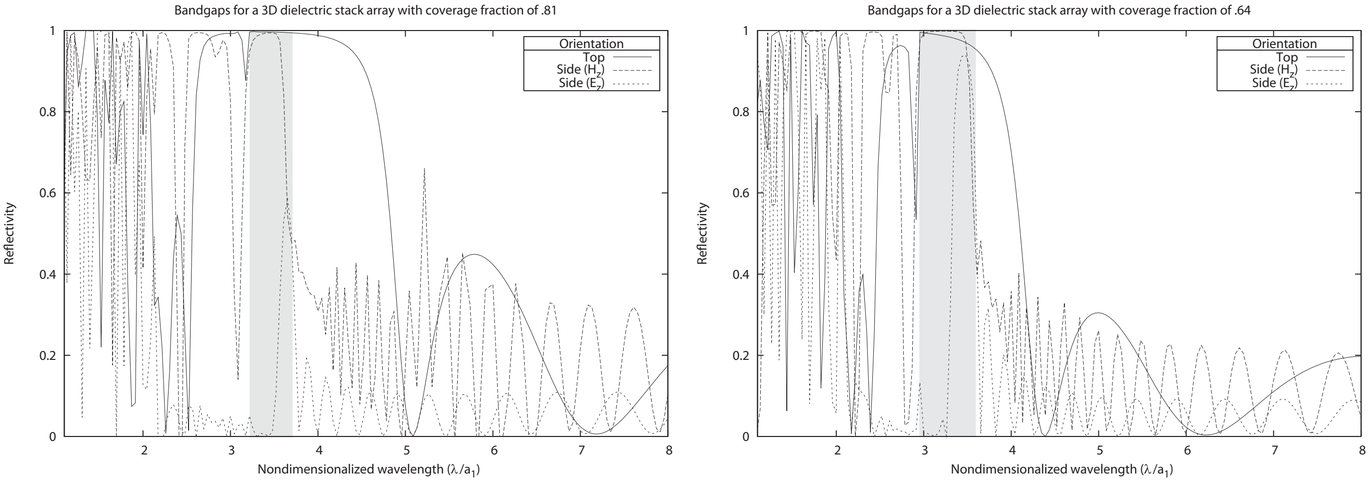

(a) 81% coverage (b) 64% coverage

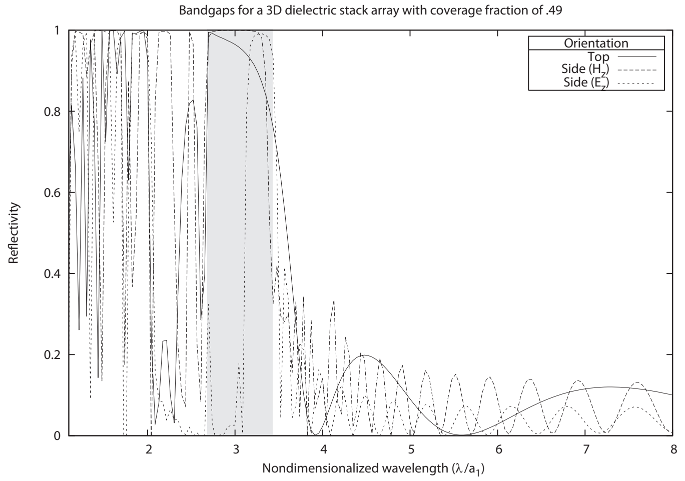

(c) 49% coverage

Figure 5-2: A comparison of the top and side bandgaps for the square array of dielectric stacks for various coverage fractions. An overlapping bandgap for all three modes is not quite opened, but the results suggest that such an overlap may be possible. Gray boxes are used to illustrate areas of high overlap.

Chapter 6

Discussion

6.1 Discussion of results

The results of chapters 4 have several exciting consequences. The first is that an array of dielectric stacks has unexpected optical properties, and there is potential for a structure with overlapping bandgaps along different axes and potentially a complete bandgap. It was also found that an array of dielectric stacks exhibit a bandgap from the top, despite the fact that the structure is partially hollow. A plausible explanation may exist for why a structure with holes completely through it can be a perfect mirror, and it is possible that the physics may be exploited to make a variety of interesting devices. If the distance between the gaps is roughly the same size as the wavelength of the incident wave, the incident wave will be diffracted as it passes though the gap. When the light is diffracted, it will spread out as it enters the structure and eventually enter one of the dielectric columns. Because the columns are quarter wavelength stacks that reflect frequencies of light that lie within the bandgap, they will perfectly reflect the light that is diffracted into them. If the dielectric constants of the components in the stack are large, the light will tend to be confined within the column due to the principle of total internal reflection. The columns are surrounded by air with the lowest possible dielectric constant, and electromagnetic waves tend to be be confined within high refractive index materials. This confinement within the column may result in the light being completely reflected.

A second observation is that the structure might be improved by switching to a hexagonal lattice or by inverting the structure so that it consists of arrays of air columns in a 1D dielectric stack. Simulating cylindrical columns may also prove advantageous. Joannopoulos observed that, for 2D photonic crystals, a square lattice of dielectric circles did not have a TM bandgap, but a hexagonal lattice of circles or a hexagonal lattice of air holes possessed a complete 2D photonic bandgap[12].

The third observation is that these structures are geometrically simple and finite yet exhibit large bandgaps. This suggests that useful structures might be able to be manufactured for applications, and controlled defects could be introduced very easily and may be used to optimize the behavior of the structure. When compared 3D photonic crystals that are known to have complete bandgaps such as dielectric spheres on a diamond lattice[22], the Yablonovite structure[13], or several of the triply periodic minimal surfaces[23], the stack array geometry is much simpler to manufacture and might be modified to be self-supporting. The columns are not self-supporting since they are surrounded by air, but it seems reasonable that if they contain enough bi-layers, they could be attached to a substrate with no effect on the optical performance of the crystal. Alternatively, a structure consisting of arrays of air columns in a 1D stack would be self-supporting.

6.2 Discussion of software

6.2.1 Philosophy on Reusable Software

One of the goals of this work has been to develop a versatile toolbox of code that can be used for a variety of simulations in place of developing many smaller stand-alone programs. Often, scientific simulations are written such that the actual simulation code, which is generally quite short, is embedded among housekeeping type functions such as input/output routines, parsing routines, mathematical procedures, etc. Although this approach is often quick to yield results, it is not at all modular and is thus difficult to debug, modify, and re-use, and, most importantly, produces code that is difficult for other scientists to use and understand. Considerable effort was invested in this this work to make sure the software was written cleanly and efficiently and is re-usable.

The design of this software is based on a grid object that can be used to write short libraries of code (similar in nature to shell scripts) that solve finite difference problems on a single processor or in parallel. Currently, libraries implementing Maxwell's equations, Cahn-Hilliard dynamics, and diffusion have been written, and the libraries themselves are short and easy to comprehend. The grid framework consists of a C++ object class and a collection of optimized macros and functions defined to operate on the grid. Grids can be written and loaded from files and there are functions that initialize the grid, set the boundary conditions, and execute macros that calculate spatial derivatives, laplacians, gradients, divergence, curls, cross products, dot products, and other mathematical operations. When run in parallel, the grid objects keep track of their neighboring grids and exchange boundary values at the end of each timestep.

Use of the grid objects will allow different simulations to be coupled. A grid object could be used for a Cahn-Hilliard phase-field simulation, and then mapped to another grid of dielectric constants which could then be analyzed using the Maxwell equations library. The result would be a simulation that measures the optical properties of a system undergoing Cahn-Hilliard evolution.

6.2.2 Implementation of Fourier Analysis

Application of Fourier analysis to the electromagnetic simulations presented in this work is an important next step that should speed up the calculation of photonic bandgaps by at least two orders of magnitude (see section 2.3). Such a speed up will make investigation of angle of incidence in 3D possible. The current approach for calculating reflectivity involves iterating over a range of incident wavelengths and measuring reflectivity from the steady-state conditions that result at each wavelength. With this method, a new simulation is run for each wavelength considered. This approach is easy to understand and implement, but very inefficient. An entire reflectivity bandgap could be calculated from one simulation of a Gaussian pulse because, unlike a plane wave that contains only one frequency, a pulse contains a wide frequency spectrum. The Fourier transform of the response of the dielectric structure to the pulse can be examined to determine the reflected power for each frequency contained in the pulse. The response function of the system can also be used to determine how the system will respond to any other input signal through the use of a convolution [Eq. 2.2].

6.2.3 A Monte Carlo Method for Optimizing Bandgaps

The problems studied in this work may lend themselves to the application of a Monte Carlo optimization method for finding geometries with unique optical properties. Analysis of the 3D structure in this work showed, among other things, that many variables characterize a system that behaves in unexpected ways. The selection of dimensions and values for variables was, in some cases, arbitrary, and it is possible that important behaviors are being missed. Additionally, much time is spent preparing and managing input files and then plotting and analyzing results. Thus a Monte Carlo method could be implemented to help automate the process of optimizing bandgaps of dielectric structures. It would be necessary to write code to generate input files and then analyze their bandgaps, perhaps by measuring the width of the bandgaps and noting their centers. This code would then assign a ranking to the structure after considering the bandgap at other angles of incidence and polarizations. A random parametric perturbation would then be made to the structure, such as a change in aspect ratio, coverage, or dielectric constants, and a new ranking would be calculated and parametric derivatives obtained. If the new structure showed improvement, it would be kept some fraction of the time related to the amount of improvement it showed, and the process would be repeated until a more desirable structure is found.

6.2.4 Public software release

A preliminary public release of the software with an open source license is anticipated in the near future after the code can be cleaned up and packaged for other users. The software will be available for Windows, Linux, and Mac OS. The initial release will contain libraries for running finite difference electromagnetic simulations, phase-field simulations, and diffusion simulations in parallel. The eventual goal of the software will be to couple these simulations with other methods such as finite element and meshless techniques to solve complex physics problems.

6.3 The Future: Multi-physics Modeling

Materials behave in complex, extremely non-linear ways, and there are important and novel material phenomenon that cannot be observed except through coupling of properties. There is a class of materials including ferroelectrics and shape memory alloys, where the application of one field could change a material's structure or geometry to effectively produce a different material. These interesting behaviors are derived from coupled interactions within the materials. The possibility of coupling many optical, electrical, and mechanical properties together in a computer simulation toolbox of reusable code will aid in the development of active materials: materials that react to their environment in intelligent ways and could be used to make novel devices, switches, and sensors. Multi-physics modeling appears to be an important field of scientific study in the computational domain in which there space for significant progress to be made.

It has shown that the realistic bounds on materials property space have been reached, and there is evidence to suggest that it is better to develop clever mixtures and geometrical configurations of materials that optimize multiple properties rather than looking for new materials that meet a strict list of design requirements[24]. Composite materials such as fiberglass, steel-reinforced concrete, and carbon-fiber weaves are being utilized for their improved mechanical properties. Two materials, each with a desirable mechanical property, are blended to create a new material with the desirable properties of each of its components. Multi-physics computational modeling seeks to expand upon this idea to create materials with novel behavior by solving simultaneously for complex interactions between mechanical, optical, electrial, magnetic, thermal, ordering, and symmetry properties. Materials that will be particularly interesting to simulating include piezoelectrics, shape memory materials (exotic shape memory polymers that react to light have recently been discovered[25]), photonic crystals that can be used to mold the flow of light[26, 27], solar cells, liquid crystals, semiconductors, and magnetic materials.

The study of multi-physics will open the door to the development of active materials: materials that, through coupling, react intelligently to their environment and can be used as novel sensors. These could be things like a light filter that can be tuned by an applied stress or electric field, materials that have a memory of their environment, or materials that respond in unique ways to light, sound, heat, or other fields. Novel geometrical constructions of these materials, such as triply periodic bicontinuous minimal surfaces, which have been shown to optimize multiple properties, will also be investigated[23, 28].

Appendix A

Reflectivity band diagrams for the 2D structure

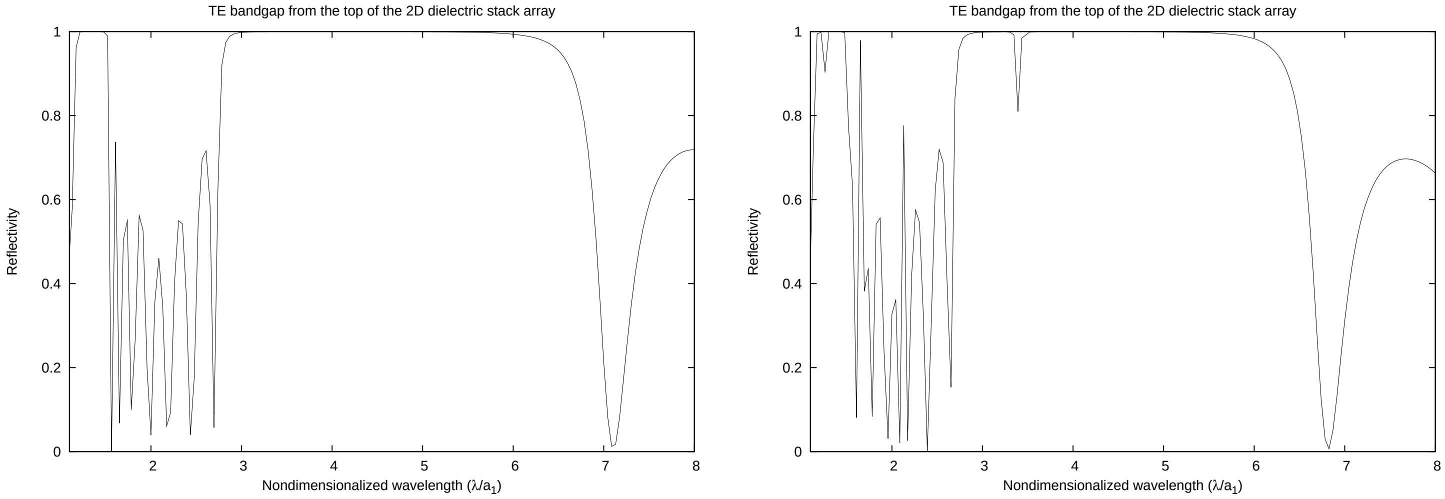

(a) 100% coverage (a 1D stack)

(b) 90% coverage

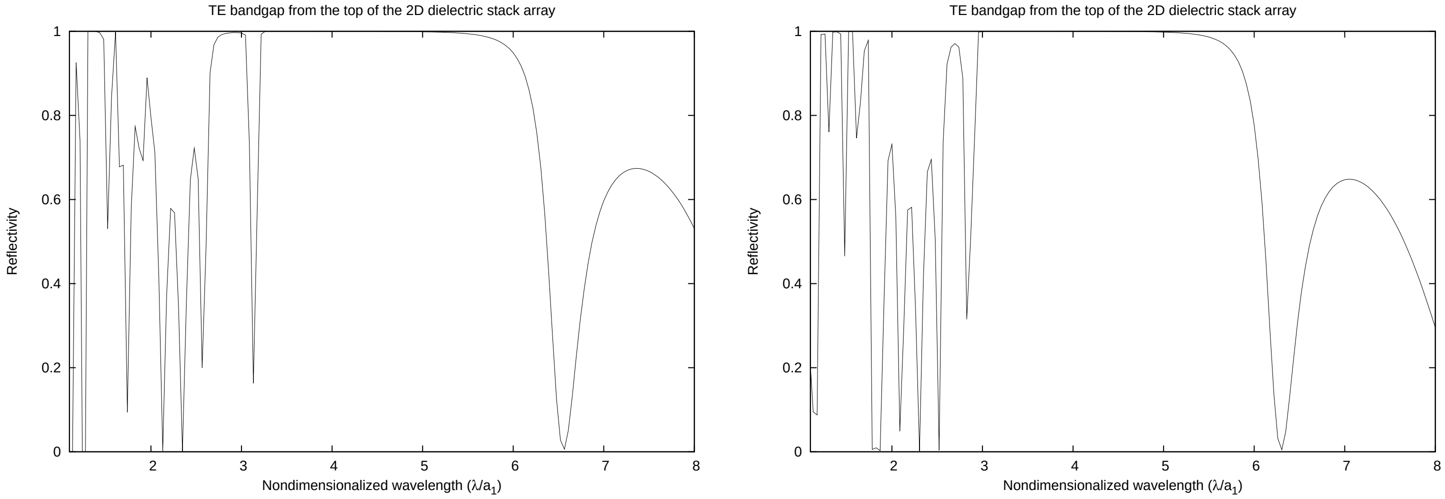

(c) 80% coverage

(d) 70% coverage

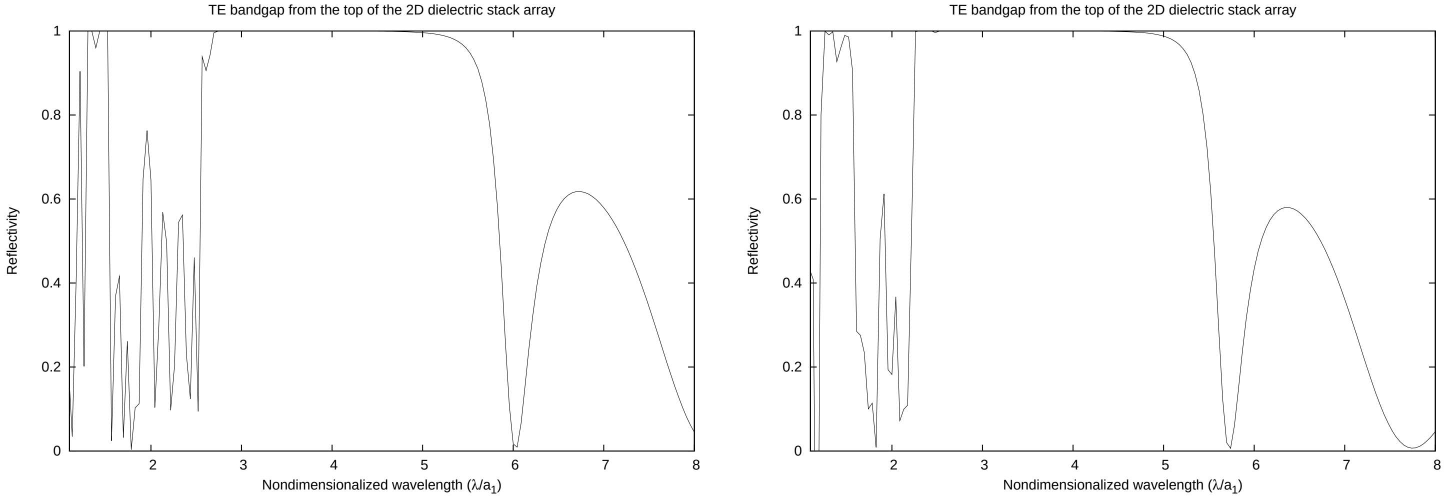

(e) 60% coverage

(f) 50% coverage

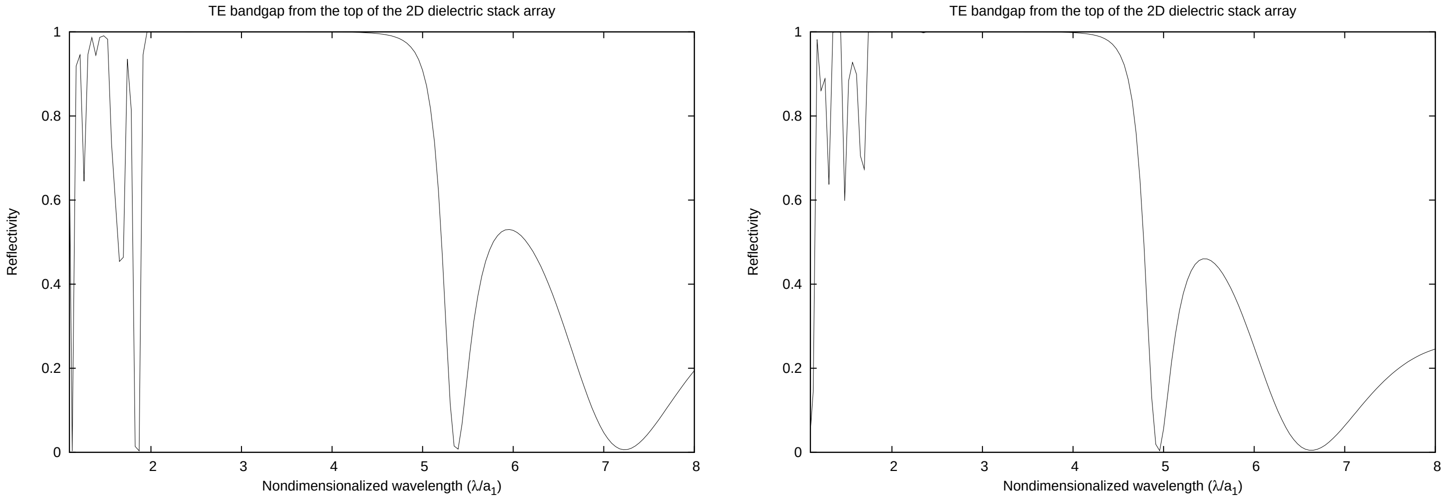

(g) 40% coverage (h) 30% coverage

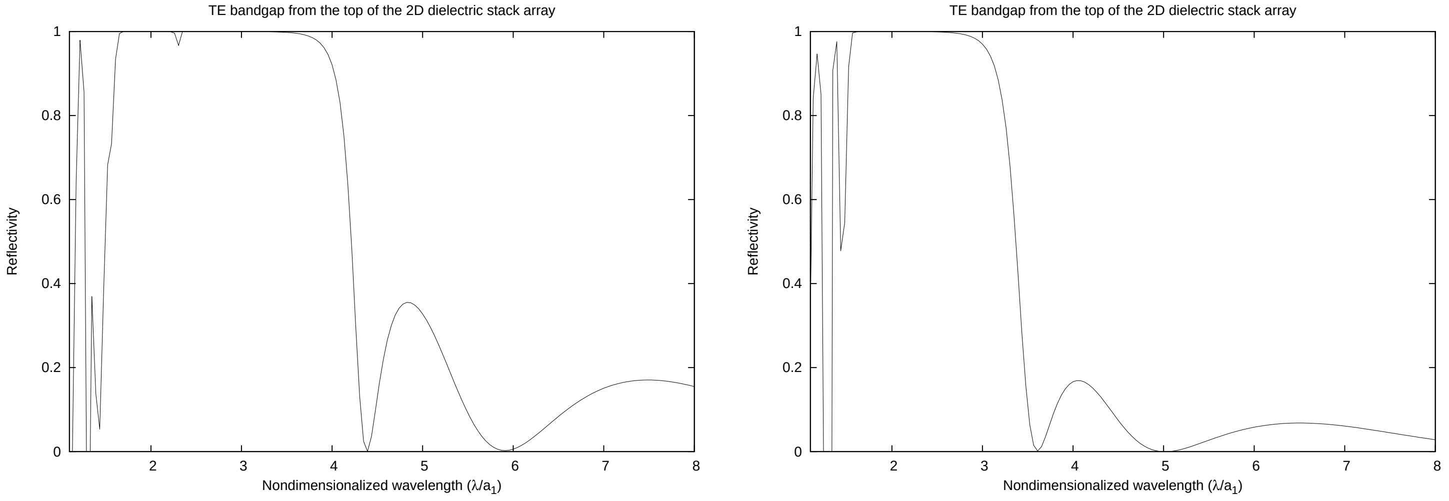

(i) 20% coverage (j) 10% coverage

Figure A-1: TE bandgap from the top direction of the 2D array of dielectric stacks with $n_1 = 4.5$ and $n_2 = 1.25$ for various coverage fractions (d/a_2).

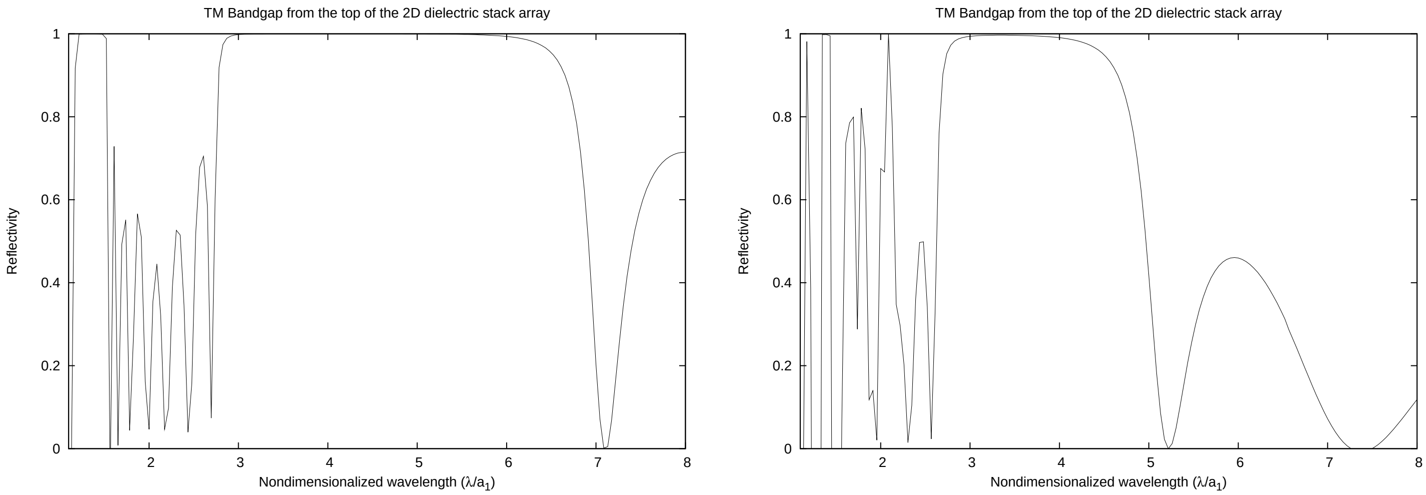

(a) 100% coverage (a 1D stack) (b) 90% coverage

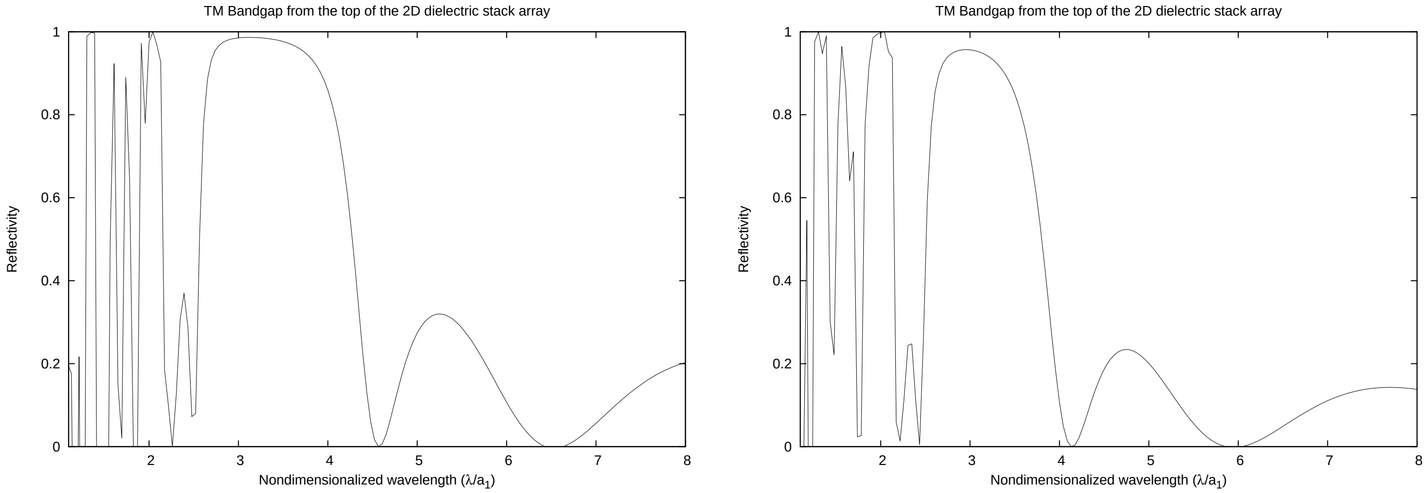

(c) 80% coverage (d) 70% coverage

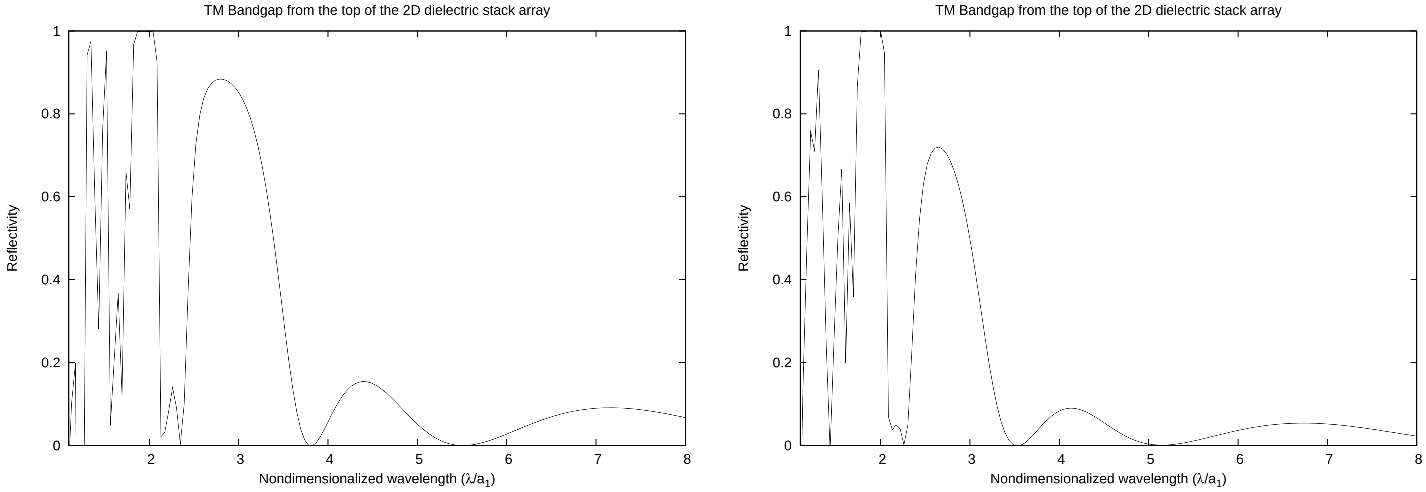

(e) 60% coverage (f) 50% coverage

Figure A-2: TM bandgap from the top direction of the 2D array of dielectric stacks with $n_1 = 4.5$ and $n_2 = 1.25$ for various coverage fractions (d/a_2).

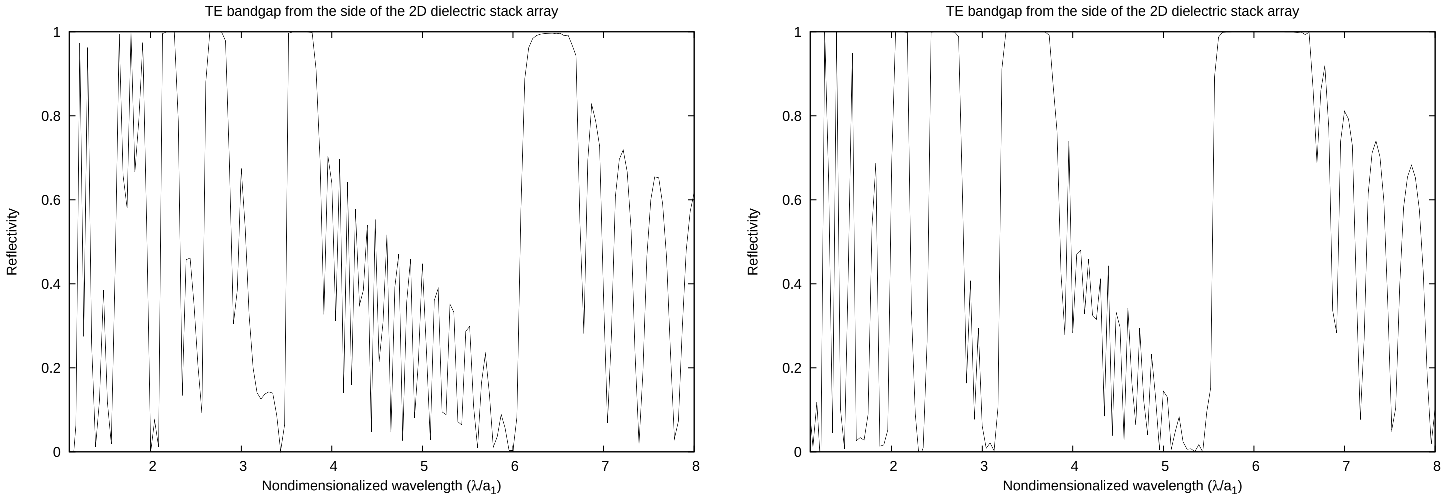

(a) 90% coverage

(b) 80% coverage

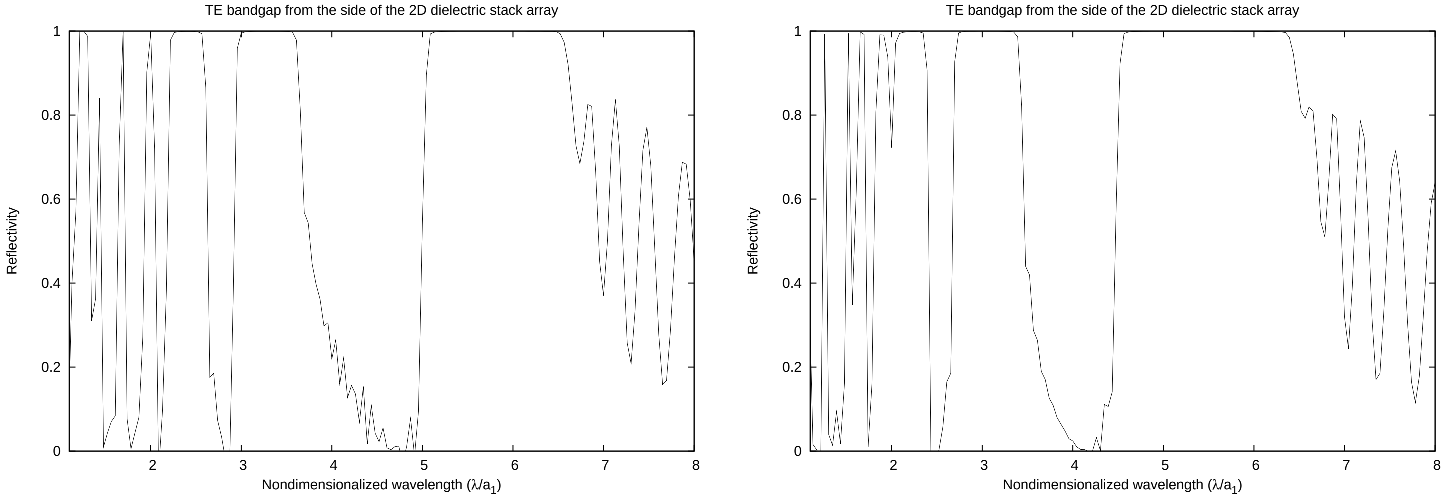

(c) 70% coverage

(d) 60% coverage

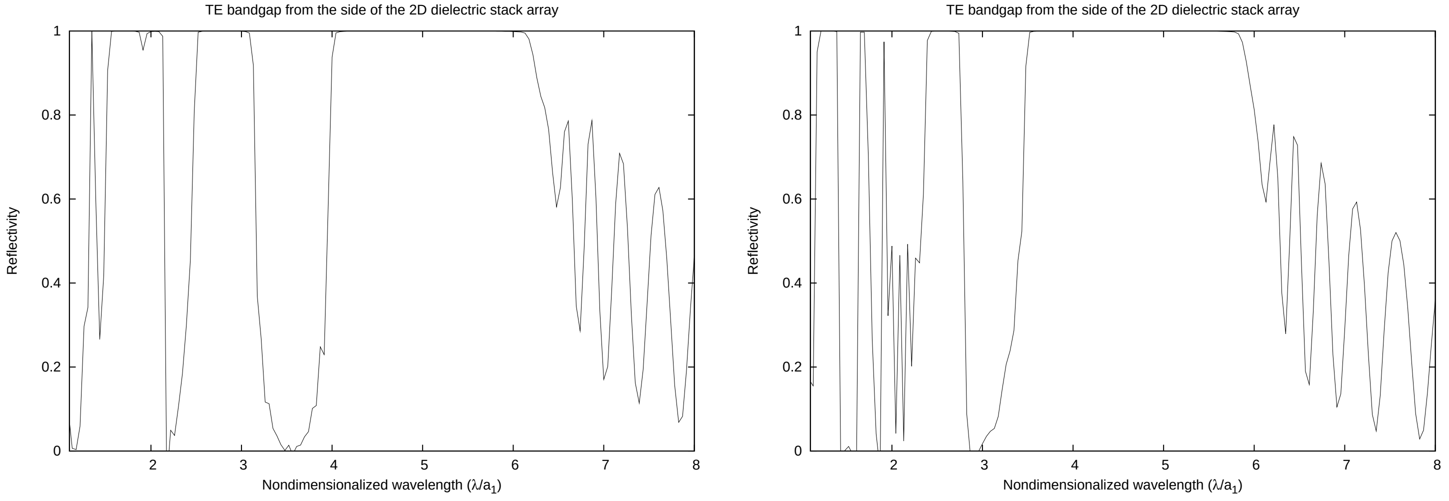

(e) 50% coverage

(f) 40% coverage

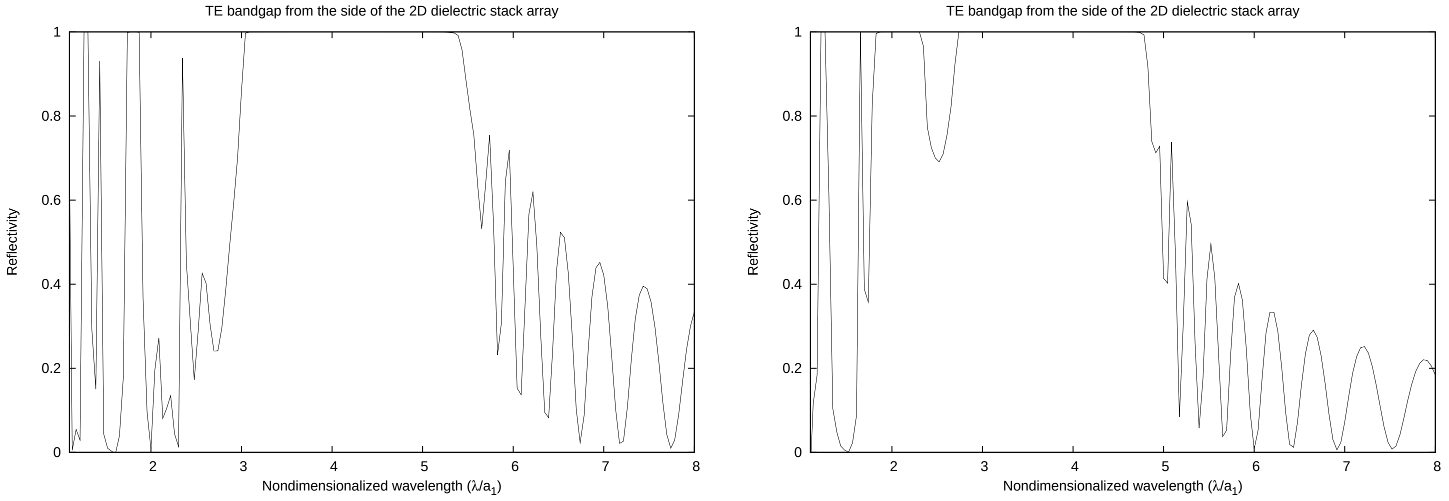

(g) 30% coverage (h) 20% coverage

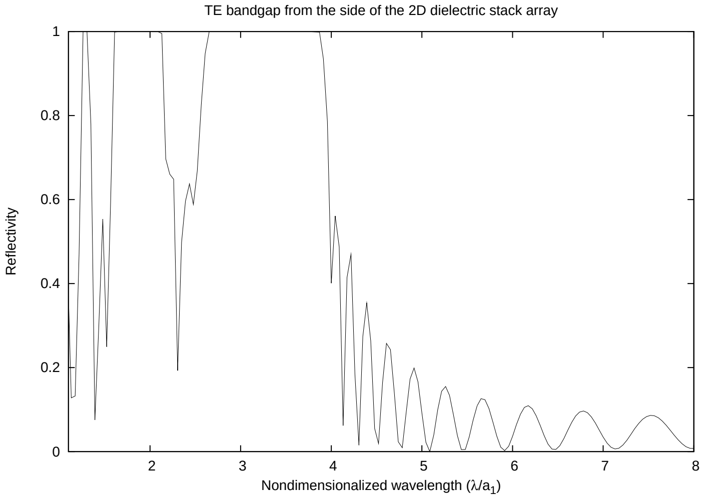

(i) 10% coverage

Figure A-3: TE bandgap from the side direction of the 2D array of dielectric stacks with $n_1 = 4.5$ and $n_2 = 1.25$ for various coverage fractions (d/a_2).

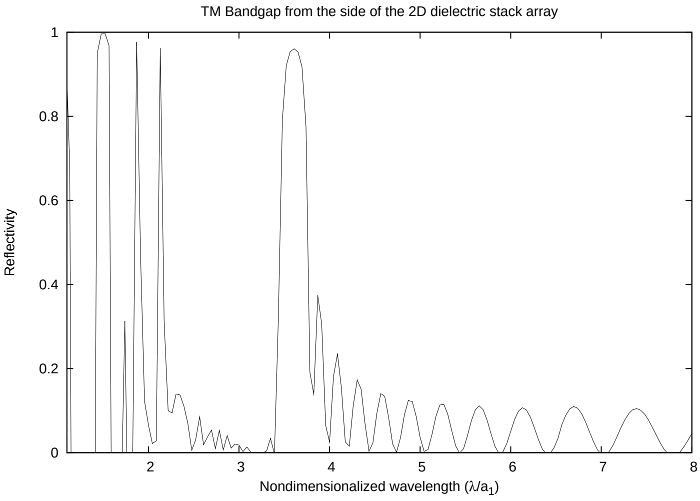

(a) 80% coverage

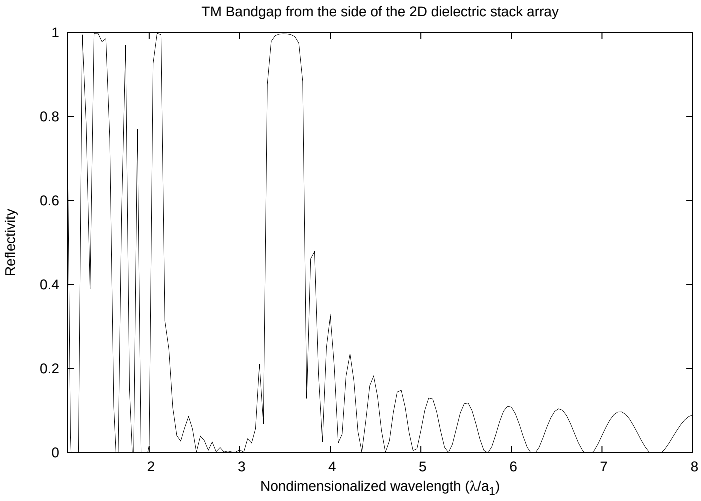

(b) 70% coverage

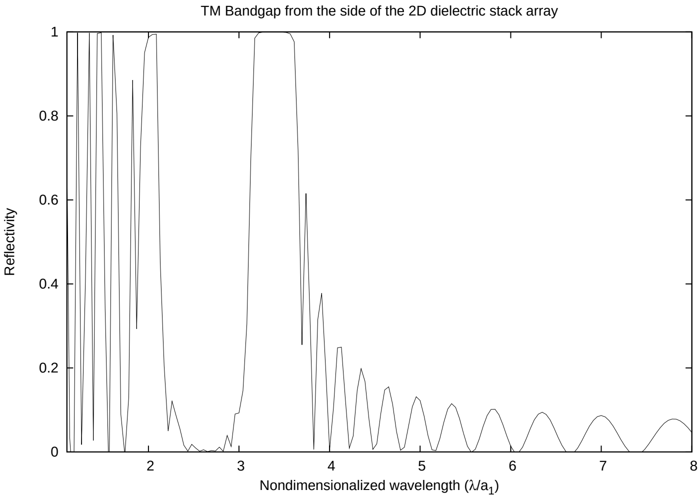

(c) 60% coverage

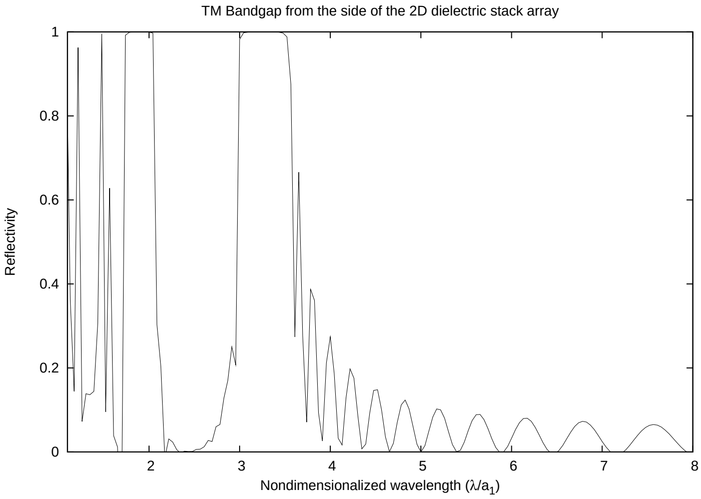

(d) 50% coverage

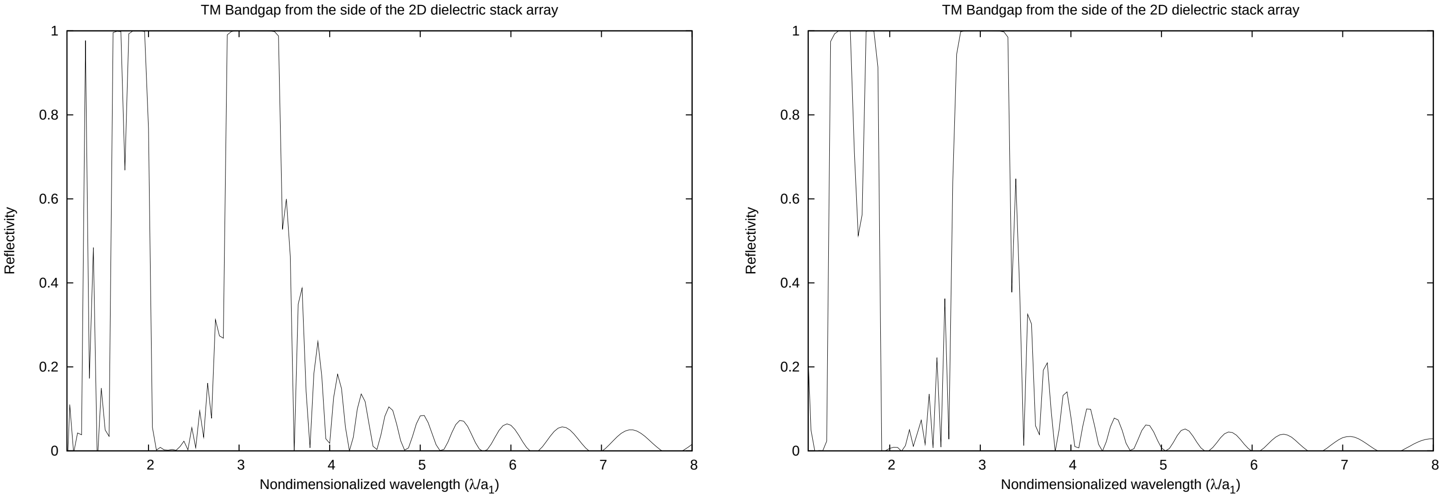

(e) 40% coverage (f) 30% coverage

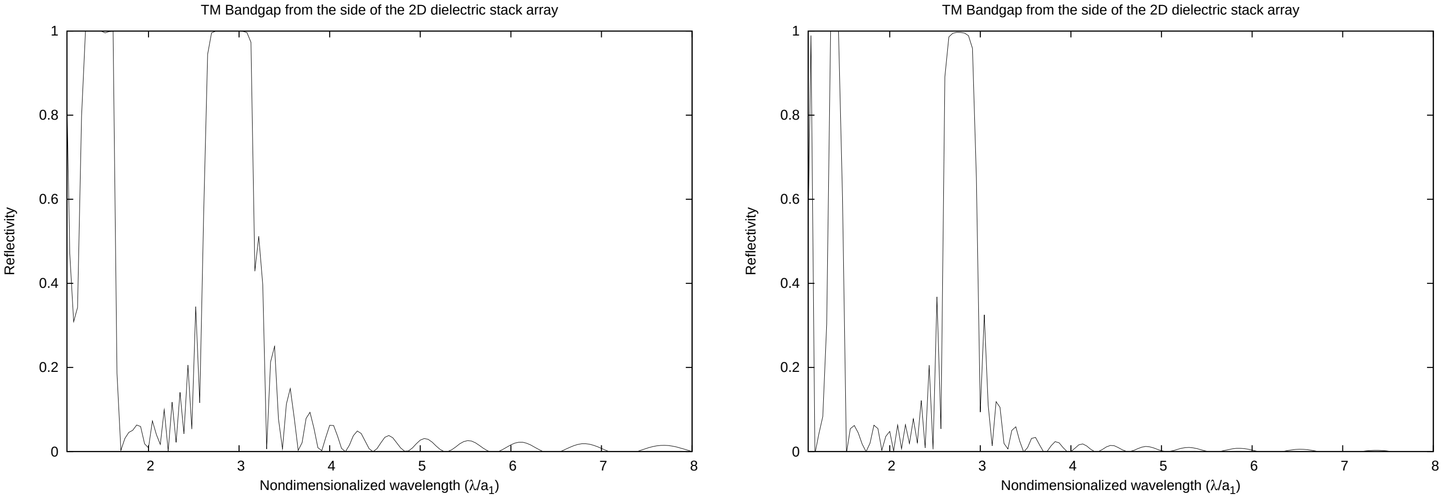

(g) 20% coverage (h) 10% coverage

Figure A-4: TM bandgap from the side direction of the 2D array of dielectric stacks with $n_1 = 4.5$ and $n_2 = 1.25$ for various coverage fractions (d/a_2).

Appendix B

Reflectivity band diagrams for the 3D structure

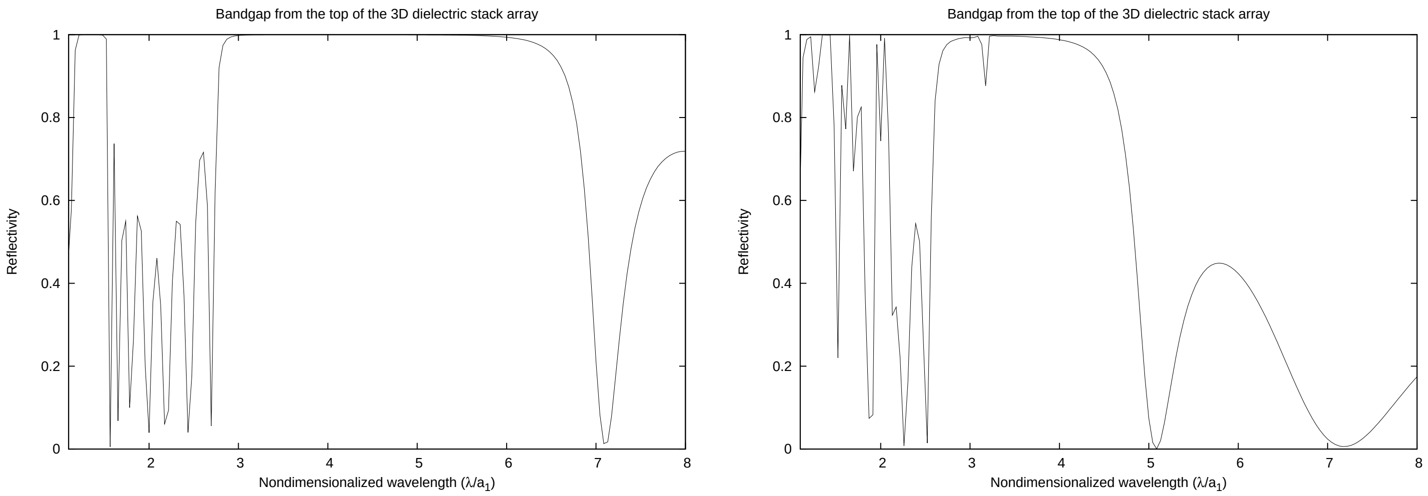

(a) 100% coverage (a 1D stack)

(b) 81% coverage

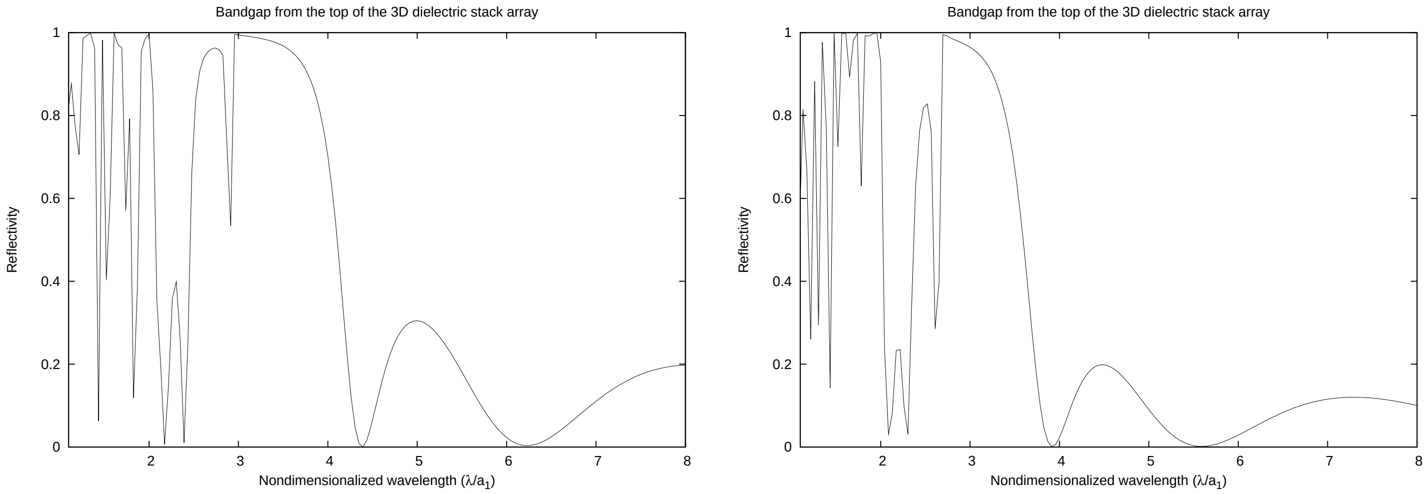

(c) 64% coverage

(d) 49% coverage

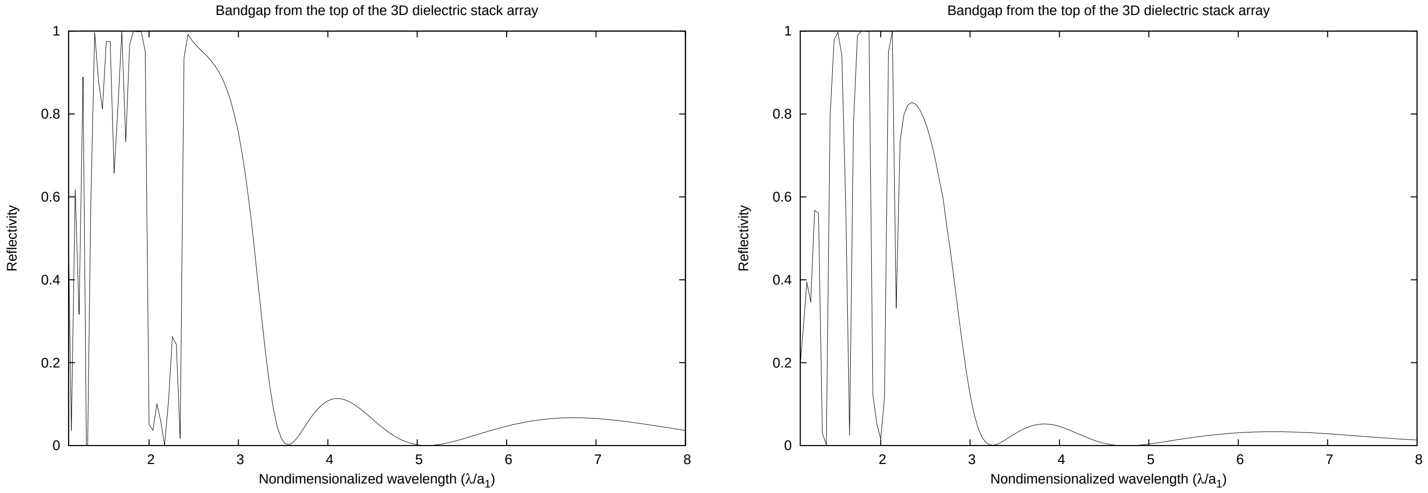

(e) 36% coverage

(f) 25% coverage

Figure B-1: Bandgap from the top direction as a function of coverage for the square array of 3D stacks with $n_1 = 4.5$ and $n_2 = 1.25$.

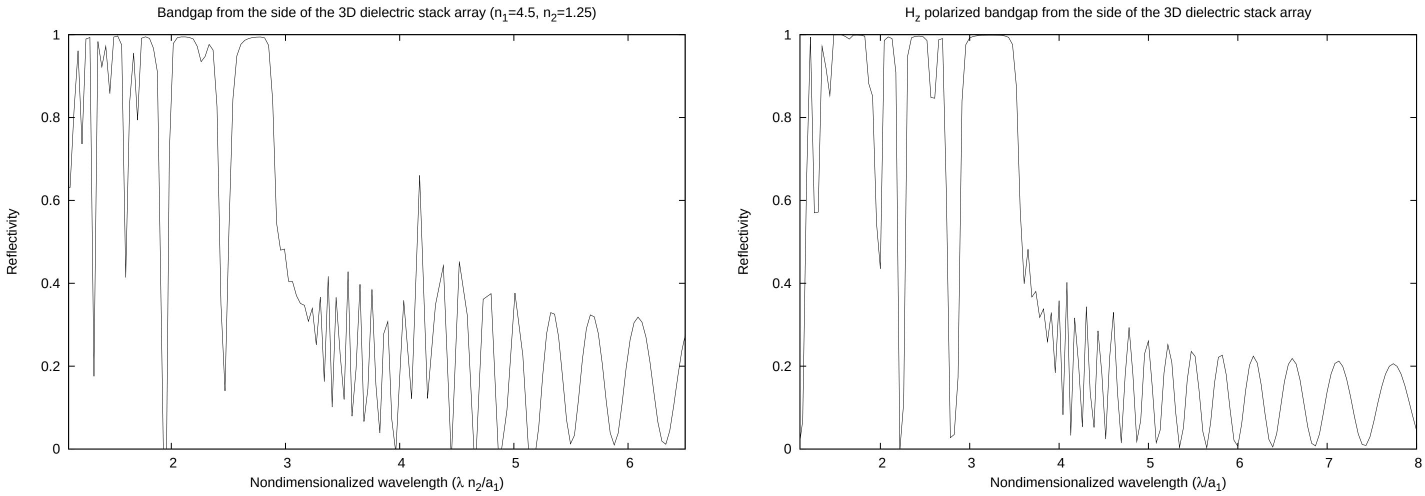

(a) 81% coverage

(b) 64% coverage

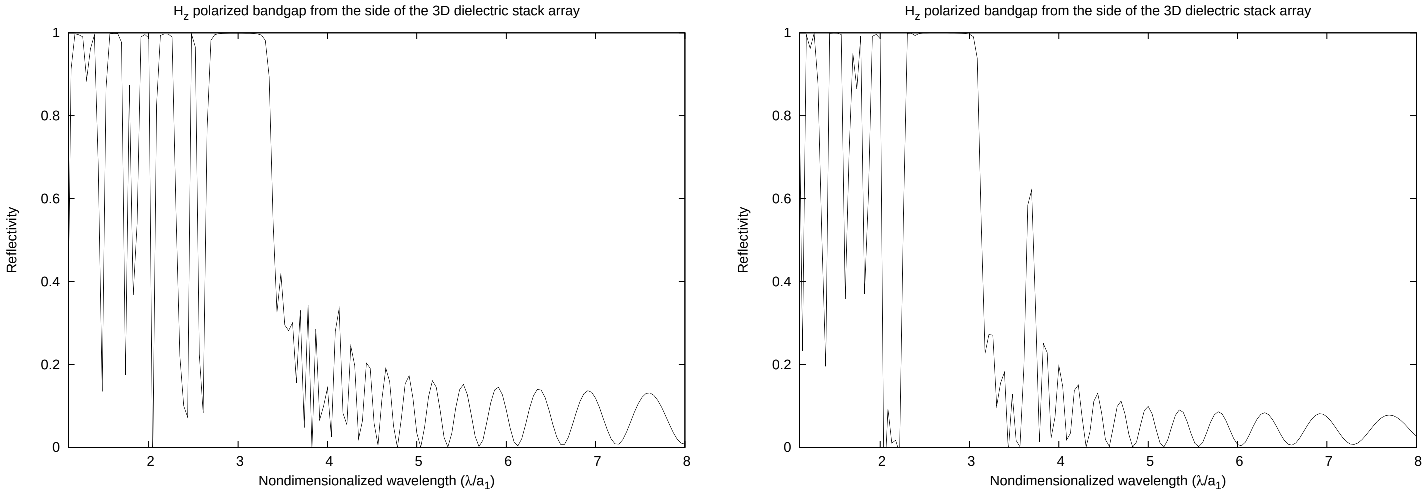

(c) 49% coverage

(d) 36% coverage

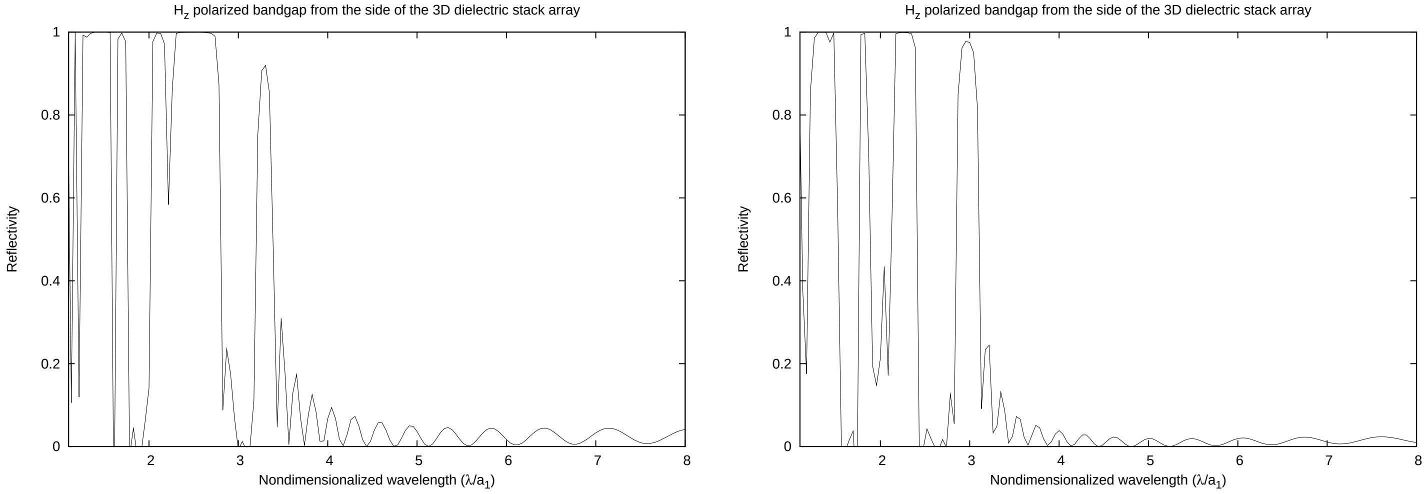

(e) 25% coverage

(f) 16% coverage

Figure B-2: H_z polarized bandgap from the side direction as a function of coverage for the square array of 3D stacks with $n_1 = 4.5$ and $n_2 = 1.25$.

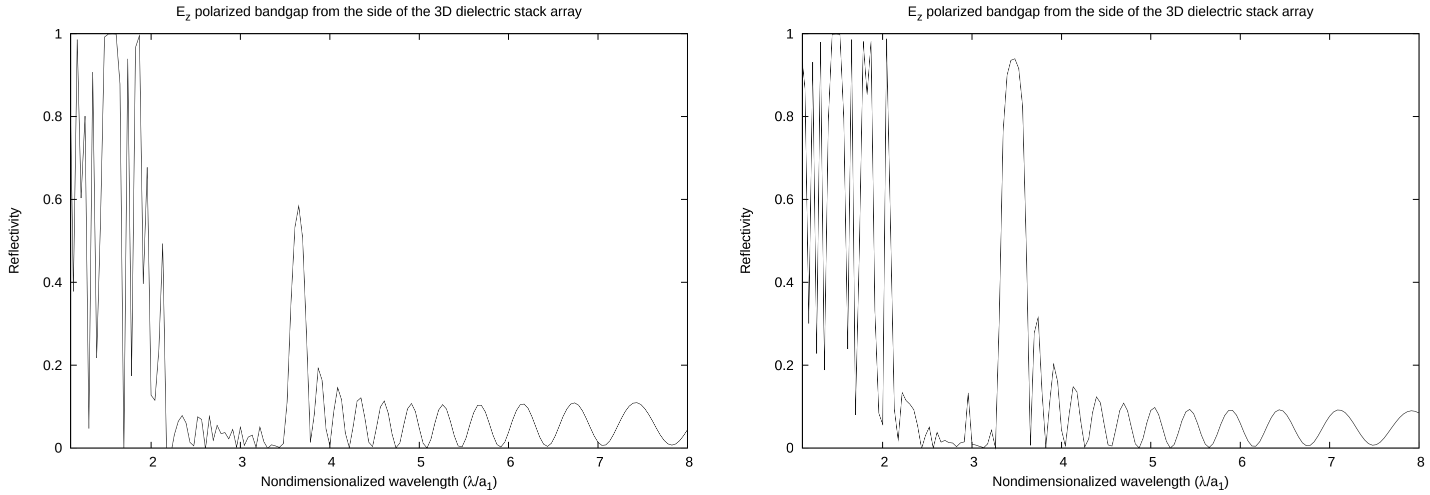

(a) 81% coverage

(b) 64% coverage

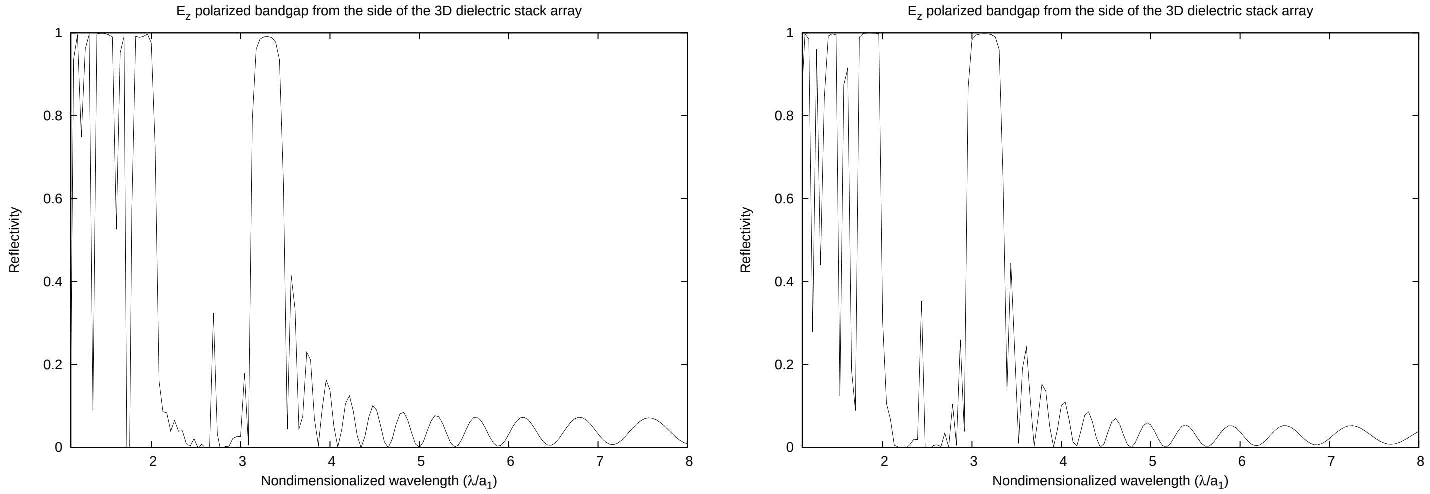

(c) 49% coverage

(d) 36% coverage

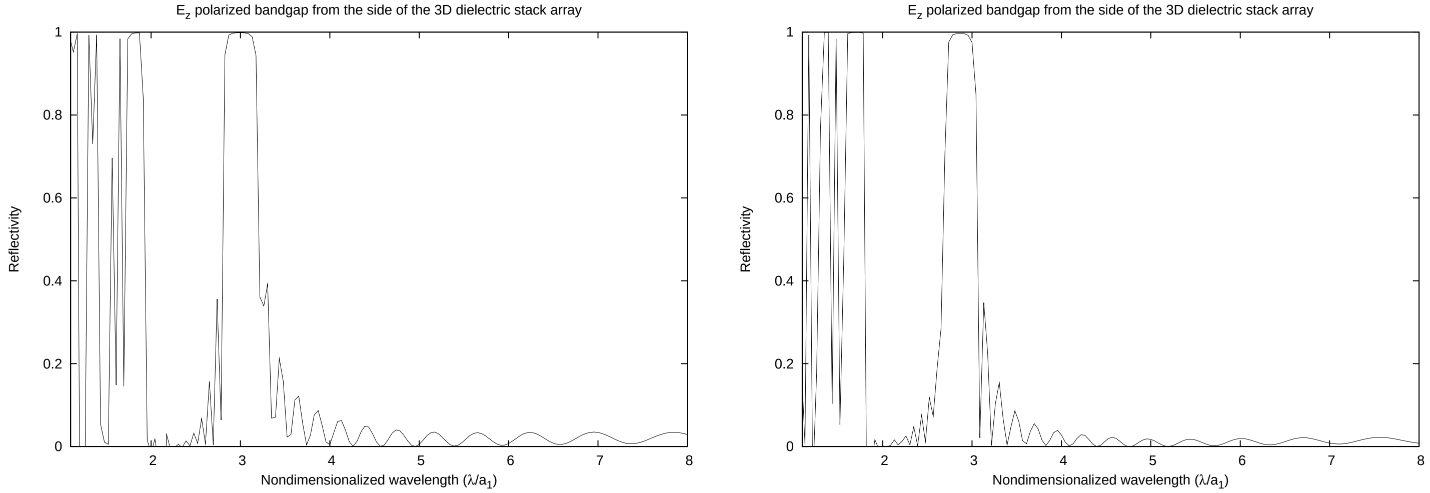

(e) 25% coverage

(f) 16% coverage

Figure B-3: E_z polarized bandgap from the side direction as a function of coverage for the square array of 3D stacks with $n_1 = 4.5$ and $n_2 = 1.25$.

References

[1] Steven G. Johnson and John D. Joannopoulos. *Photonic Crystals: The Road from Theory to Practice.* Kluwer Academic Publishers, 2002.

[2] Allen Taflove and Susan C. Hagness. *Computational Electrodynamics: The Finite-Difference Time-Domain Method.* Artech House, 2000.

[3] Basil Mahon. *The Man Who Changed Everything.* John Wiley and Sons, Inc., 2003.

[4] John David Jackson. *Classical Electrodynamics.* John Wiley and Sons, Inc., 1999.

[5] Jin Au Kong. *Electromagnetic Wave Theory.* EMW Publishing, 2000.

[6] Alfred Owen Aldridge. *Benjamin Franklin Philosopher and Man.* J.B. Lippincott Company, 1965.

[7] Erwin Kreyszig. *Advanced Engineering Mathematics.* John Wiley and Sons Inc., 1999.

[8] Marko Loncar, Tomoyuki Yoshie, and Axel Scherer. Low-threshold photonic crystal laser. *Applied Physics Letters*, 81:2680–2682, 2002.

[9] Susumu Noda, Alongkarn Chutinan, and Masahiro Imada. Trapping and emission of photons by a single defect in a photonic bandgap structure. *Nature*, 407:608–610, 2000.

[10] Y Sugimoto, Y Tanaka, N Ikeda, K Kanamoto, Y Nakamura, S Ohkouchi, H Nakamura, K Inoue, H Sasaki, Y Watanabe, K Ishida, H Ishikawa, and K Asakawa. Two dimensional semiconductor-based photonic crystal slab waveguides for ultra-fast optical signal processing devices. *IEICE Transactions on Electronics*, E87C:316–327, 2004.

[11] DR Smith, WJ Padilla, DC Vier, SC Nemat-Nasser, and S Schultz. Composite medium with simultaneously negative permeability and permittivity. *Physical Review Letters*, 84:4184–4187, 2000.

[12] John D. Joannopoulos, Robert D. Meade, and Joshua N. Winn. *Photonic Crystals: Molding the Flow of Light.* Princeton University Press, 1995.

[13] E Yablonovitch, TJ Gmitter, and KM Leung. Photonic band-structure - the face-centered-cubic case employing nonspherical atoms. *Physical Review Letters*, 67:2295–2298, 1991.

[14] H. Joseph Weaver. *Applications of Discrete and Continuous Fourier Analysis.* John Wiley and Sons, Inc., 1983.

[15] Kane S. Yee. Numerical solution of initial boundary value problems involving maxwell's equations in isotropic media. *IEEE Transactions on Antennas and Propagation*, 14:302–307, 1966.

[16] Jean-Pierre Berenger. A perfectly matched layer for the absorption of electromagnetic waves. *Journal of Computational Physics*, 114:185–200, 1994.

[17] Dennis M. Sullivan. *Electromagnetic Simulation Using the FDTD Method.* IEEE Press, 2000.

[18] Karlene R. Maskaly. *Computational Study and Analysis of Structural Imperfections in 1D and 2D Photonic Crystals.* PhD thesis, MIT, 2005.

[19] David Halliday, Robert Resnick, and Jearl Walker. *Fundamentals of Physics.* John Wiley and Sons Inc, 2001.

[20] Jelena Vuckovic, Matthew Pelton, Axel Scherer, and Yoshihisa Yamamoto. Optimization of three-dimensional micropost microcavities for cavity quantum electrodynamics. *Physical Review A*, 66, 2002.

[21] Matthew Pelton, Jelena Vuckovic, Glenn Solomon, Charles Santori, Bingyang Zhang, Jocelyn Plant, and Yoshihisa Yamamoto. An efficient source of single photons: a single quantum dot in a micropost microcavity. *Physica E*, 17:564–567, 2003.

[22] KM Ho, CT Chan, and CM Soukoulis. Existence of a photonic gap in periodic dielectric structures. *Physical Review Letters*, 65:3125–3155, 1990.

[23] Alan H. Schoen. Infinite periodic minimal surfaces without self-intersections. *NASA Technical Note*, 1969.

[24] M. F. Ashby. Multi-objective optimization in material design and selection. *Acta Materialia*, 48:359–369, 2000.

[25] Andreas Lendlein, Hongyan Jiang, Oliver Junger, and Robert Langer. Light-induced shape-memory polymers. *Nature*, 434(7035):879–882, 2005.

[26] D.N. Chigrin, A.V. Lavrinenko, D.A. Yarotsky, and S.V. Gaponenko. Observation of total omnidirectional reflection from a one-dimensional dielectric lattice. *Applied Physics A*, 68:25–28, 1999.

[27] Emmanuel Centeno and David Cassagne. Graded photonic crystals. *Optics Letters*, 30:2278–2280, 2005.

[28] S. Torquato, S. Hyun, and A. Donev. Multifunctional composites: Optimizing microstructures for simultaneous transport of heat and electricity. *Physical Review Letters*, 89(26), 2002.